

Extended finite element simulation of fracture network propagation in formation containing frictional and cemented natural fractures



XiaoLong Wang^a, Fang Shi^{a,b}, Chuang Liu^a, DeTang Lu^a, He Liu^c, HengAn Wu^{a,*}

^a CAS Key Laboratory of Mechanical Behavior and Design of Materials, Department of Modern Mechanics, University of Science and Technology of China, Hefei, Anhui 230027 China

^b Faculty of Mechanical & Material Engineering, Huaiyin Institute of Technology, Huai'an, Jiangsu 223003 China

^c PetroChina Research Institute of Petroleum Exploration & Development, 20 Xueyuan Road, Haidian District, Beijing 100083 China

ARTICLE INFO

Keywords:

Shale
Hydraulic fracturing
Frictional natural fracture
Cemented natural fracture
Fracture network
XFEM

ABSTRACT

Shale gas reservoirs often need hydraulic fracturing treatments to create complex fracture network to enhance production. Frictional and cemented natural fractures are often contained in shale formations. The interactions between the hydraulic fractures and these two types of pre-existing natural fractures are different. In this study, we established a two-dimensional fluid-solid coupled hydraulic fracturing model using the extended finite element method (XFEM) to simulate the interactions between hydraulic fractures and natural fractures, and further the formation of fracture network. The results show that when a hydraulic fracture intersects with a natural fracture, the hydraulic fracture may be arrested and propagate along the direction of natural fracture, or cross the natural fracture without being affected. For the frictional natural fractures, the intersection angle, frictional coefficient, stress anisotropy and rock tensile strength have a significant influence on creating fracture network. It is found that decreasing stress difference and interfacial friction, or increasing rock tensile strength may lead to more complex fracture network. For the cemented natural fractures, the intersection angle and the ratio of cement toughness and rock toughness play critical roles in the creation of fracture network. Smaller intersection angle and cement toughness of natural fractures and larger rock fracture toughness often lead to more complex fracture network. In addition, for the same initial geometrical configuration of natural fractures, hydraulic fracturing often leads to more complex fracture network in formations containing frictional natural fractures compared with formations containing cemented natural fractures. These findings offer new insights into the nature and degree of fracture complexity, helping to optimize hydraulic fracturing design in shale gas reservoirs.

1. Introduction

As a kind of unconventional energy sources, shale gas trapped in shale formation has gotten more attention around the world in recent years. Because of the extremely low permeability, shale formations often need hydraulic fracturing treatments for economical production. Recently, the multistage hydraulic fracturing in horizontal wells has been widely used to enhance well production in shale gas reservoirs (Liu et al., 2015, 2016; Shi et al., 2016; Wang et al., 2016a). A large number of natural fractures (NFs) exist in shale formations, which have a great influence on the hydraulic stimulation. The interactions between the hydraulic fractures (HFs) and the pre-existing NFs often promote the formation of complex fracture network. The production of the reservoir is directly related to the complexity of the created fracture network. It is obliged to correctly predict the complex fracture network

development during fracturing treatments to optimize stimulation design and completion strategy.

A good deal of theoretical and experimental investigations have been performed to analyze the interactions between HFs and NFs (Beugelsdijk et al., 2000; Blanton, 1982, 1986; Chuprakov et al., 2013; Daneshy, 1974; Gu and Weng, 2010; Gu et al., 2011; Jeffrey et al., 2015; Lamont and Jessen, 1963; Olson et al., 2012; Potluri et al., 2005; Renshaw and Pollard, 1995; Warpinski and Teufel, 1987; Zhou et al., 2008). Blanton (1982) conducted a lot of experiments on naturally fractured hydrostone blocks and Devonian shale to inspect the effect of intersection angle and differential stress on the HF propagation. Through conducting mineback experiments, Warpinski and Teufel (1987) studied the influence of geologic discontinuities on the HF propagation and found that the HF crossed the existing fracture at high intersection angle and high differential stress. Based on the theory of

* Corresponding author.

E-mail address: wuha@ustc.edu.cn (H. Wu).

linear-elastic fracture mechanics, Renshaw and Pollard (1995) developed a simple criterion to predict whether the growing HF will cross or terminate at the frictional NF which is orthogonal to the approaching fracture. The Renshaw and Pollard criterion was extended by Gu and Weng (2010) for non-orthogonal intersection angles and the extended criterion was validated for extensive intersection angles through laboratory experiments (Gu et al., 2011).

Because of the limitation of the theoretical and experimental investigations, many researchers have developed various numerical methods to simulate the interactions between HFs and NFs. Recently, the most extensively used numerical techniques for modeling hydraulic fracturing are the displacement discontinuity method (DDM), the distinct element method (DEM), the finite element method (FEM), and the extended finite element method (XFEM). With the advantages of high computational efficiency and accuracy, the DDM has been developed to study the interactions between HFs and frictional NFs (Zhang and Jeffrey, 2006, 2012, 2014; Zhang et al., 2009), and the creation of complex fracture network in naturally fractured reservoirs (Kresse et al., 2013; Olson and Taleghani, 2009; Ren et al., 2016; Weng et al., 2011, 2014; Wu and Olson, 2015; Zeng and Yao, 2016). However, the DDM has some difficulties in solving the deformation of inhomogeneous and anisotropic materials. Meanwhile, the 2D and 3D fracturing models based on the DEM have also been used to investigate the effects of injection rate and fluid viscosity on hydraulic fracturing in naturally fractured rock, and the mechanism of fracture network propagation in the shale formation containing plenty of pre-existing NFs (Damjanac et al., 2010; De Pater and Beugelsdijk, 2005; Nagel et al., 2011; Zou et al., 2016). Since the rock mass is treated as a combination of discrete blocks connected by faults in the DEM, it is easy to simulate the intersections between HFs and NFs, and the formation of complex fracture network. However, the computational cost of DEM is very expensive when computational domain is large. The FEM is an effective and widely used numerical technique. Nevertheless, simulation of hydraulic fracturing using FEM is very time-consuming since it needs remeshing with fracture propagation (Omidi et al., 2015). By making the fractures only propagate along the edges of cohesive elements, the FEM in conjunction with the cohesive element method can explicitly simulate the intersection of HF and NF without the need of remeshing, and then the computational cost is decrease (Chen et al., 2017; Gonzalez-Chavez et al., 2015; Guo et al., 2015). However, in this case the propagation paths of fractures are restricted either. In order to overcome the shortcomings of FEM, the XFEM has been proposed, which can be regarded as an improvement of the FEM. The numerical model based on the XFEM has been employed to study the interactions of the HF with the cemented NFs (Dahi-Taleghani and Olson, 2011, 2014) and the frictional NFs (Khoei et al., 2015; Shi et al., 2017).

From the above discussion it should be clear that the NFs in rock formation usually can be divided into two types: frictional and cemented NFs. The division of the two types of NFs mainly depends on the degree of difficulty of the slip along the fracture interfaces. With a smaller cohesion of interfaces, slip along the fracture interfaces often occurs during the interactions of HFs and NFs. In this case, the NFs usually can be treated as frictional NFs (Blanton, 1982; Gu et al., 2011; Jang et al., 2016; Renshaw and Pollard, 1995; Wasantha and Konietzky, 2016; Wu and Olson, 2015; Zhang and Jeffrey, 2006, 2014). However, when the fracture interfaces are perfectly bonded together by cements with large fracture strength, slip along the fracture interfaces is difficult to occur during the interactions of HFs and NFs. In this case, the NFs can be generally treated as cemented NFs. (Dahi-Taleghani and Olson, 2011, 2014; Xie et al., 2016). Note that there is no strict boundary between the two types of NFs, since the frictional NFs can convert to cemented NFs when the cohesion of interfaces is large enough to prevent the interfaces from slipping and the cemented NFs can convert to frictional NFs when the fracture interfaces debonding occurs during the interaction process. (In this paper, we assume that the cohesion of interfaces of frictional NFs is zero and no debonding occurs during the

interaction process for cemented NFs). Both the frictional and cemented NFs can serve as weak paths for HFs beginning and/or diversion and promote the formation of fracture network. Due to their different mechanical properties, the processes of the interactions between the HFs and the two types of NFs are substantially different. However, there is no uniform hydraulic fracturing model simultaneously incorporating the two types of NFs, and the different effects of the two types of NFs on the propagation of HFs and the generation of fracture network have not been investigated in depth.

In this paper, a fully coupled 2D hydraulic fracturing model based on the XFEM is established to simulate the creation of fracture network in shale formations containing frictional and cemented NFs. The key physical mechanisms such as rock deformation, propagation of fractures, interactions of HFs and NFs, fluid flow within fractures, contact conditions of fractures and stress shadow effect are all taken into account. Additionally, the different HF/NF interaction criterions for both types of NFs are also incorporated in the model. The effects of the two types of NFs on the HFs propagation and the creation of fracture network are compared.

2. Problem formulation

2.1. Governing equations of hydraulic fracturing problems

As illustrated in Fig. 1, consider a 2D homogeneous, isotropic, linear elastic medium Ω containing a hydraulically driven fracture Γ_{HF} filled with fluid injected at a constant rate of Q_0 . Because of the low permeability of shale formations, the impact of pore pressure of the formation on the fracture propagation is not obvious and the medium Ω can be assumed as impermeable medium. The domain also contains a pre-existing NF Γ_{NF} which may be intersected by the HF. The prescribed tractions \mathbf{t} and the displacements $\bar{\mathbf{u}}$ are imposed on the boundary Γ_t and Γ_u , respectively. The unit outwards normal vectors of the HF Γ_{HF} and the NF Γ_{NF} are denoted by $\mathbf{n}_{\Gamma_{HF}}$ and $\mathbf{n}_{\Gamma_{NF}}$, respectively. For simplicity, we assume that the fluid is incompressible and the propagation of the fracture is a quasi-static process. The fluid lag and the fluid leak-off into the surrounding rock formation are not considered in our model.

The equilibrium equation of the domain and the boundary conditions can be expressed as

$$\nabla \cdot \boldsymbol{\sigma} + \mathbf{b} = 0, \quad \text{in } \Omega \tag{1}$$

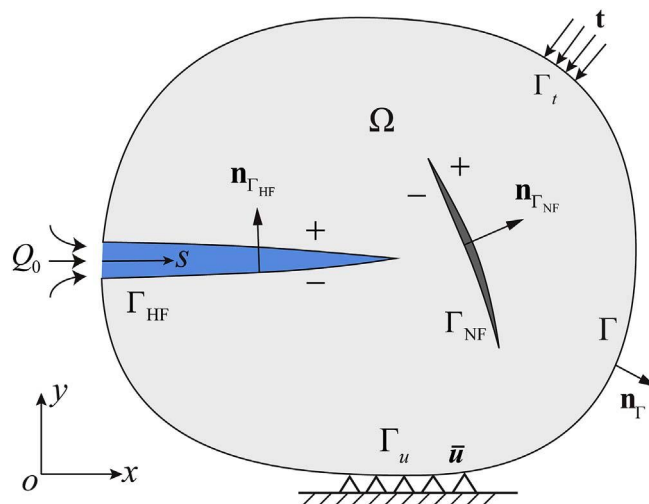


Fig. 1. Illustration of a domain containing a HF and a NF.

$$\begin{cases} \mathbf{u} = \bar{\mathbf{u}} & \text{on } \Gamma_u \\ \boldsymbol{\sigma} \cdot \mathbf{n} = \mathbf{t} & \text{on } \Gamma_t \\ \boldsymbol{\sigma} \cdot \mathbf{n}_{\Gamma_{HF}} = p \mathbf{n}_{\Gamma_{HF}} & \text{on } \Gamma_{HF} \\ \boldsymbol{\sigma} \cdot \mathbf{n}_{\Gamma_{NF}} = \mathbf{t}^{\text{cont}} & \text{on } \Gamma_{NF} \end{cases} \quad (2)$$

where $\boldsymbol{\sigma}$ and \mathbf{b} are the Cauchy stress tensor and the body force, respectively; p represents the fluid pressure, \mathbf{t}^{cont} is the contact traction vector acting on the surfaces of NF Γ_{NF} .

2.2. Crack propagation criterion

The classical maximum circumferential tensile stress criterion is adopted to calculate the fracture propagation in the rock formation. If the equivalent stress intensity factor K_e is greater than or equal to the fracture toughness of the rock formation, K_{IC} , the fracture will propagate. The equivalent stress intensity factor K_e is calculated as (Erdogan and Sih, 1963):

$$K_e = \cos \frac{\alpha}{2} \left(K_I \cos^2 \frac{\alpha}{2} - \frac{3K_{II}}{2} \sin \alpha \right) \quad (3)$$

where K_I and K_{II} represents the stress intensity factors for mode I and II. They are calculated by the domain forms of the interaction integral method in this paper. α is the fracture propagation angle which is defined in the local polar coordinate system at the fracture tip

$$\alpha = 2 \arctan \left(\frac{-2K_{II}/K_I}{1 + \sqrt{1 + 8(K_{II}/K_I)^2}} \right) \quad (4)$$

When a HF encounters a frictional NF, three scenarios of fracture propagation may occur (Gu et al., 2011), as shown in Fig. 2. First, the HF may be arrested by the frictional NF and the NF is dilated by fracturing fluid. Then the HF grows along the NF, forming a T-shaped fracture, as shown in Fig. 2(a). In the second case, the HF may cross the frictional NF and propagate along the direction of the maximum horizontal stress. The frictional NF remains closed during the intersection, as shown in Fig. 2(b). In the third case, after the HF crosses the frictional NF, the fracturing fluid dilates the NF and the HF branches into the NF, as shown in Fig. 2(c).

In this paper, the extended Renshaw and Pollard criterion (Gu et al., 2011) is adopted to determine the cross/arrest behavior between the

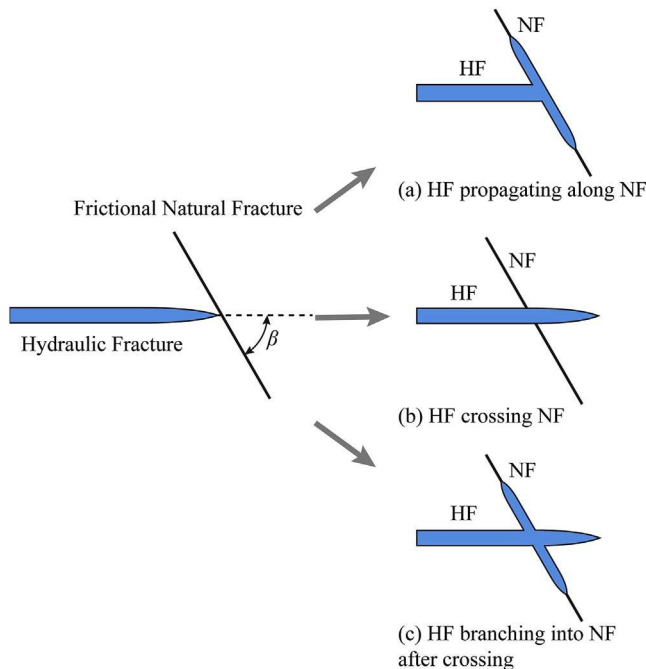


Fig. 2. Schematic of interaction process between a HF and a frictional NF.

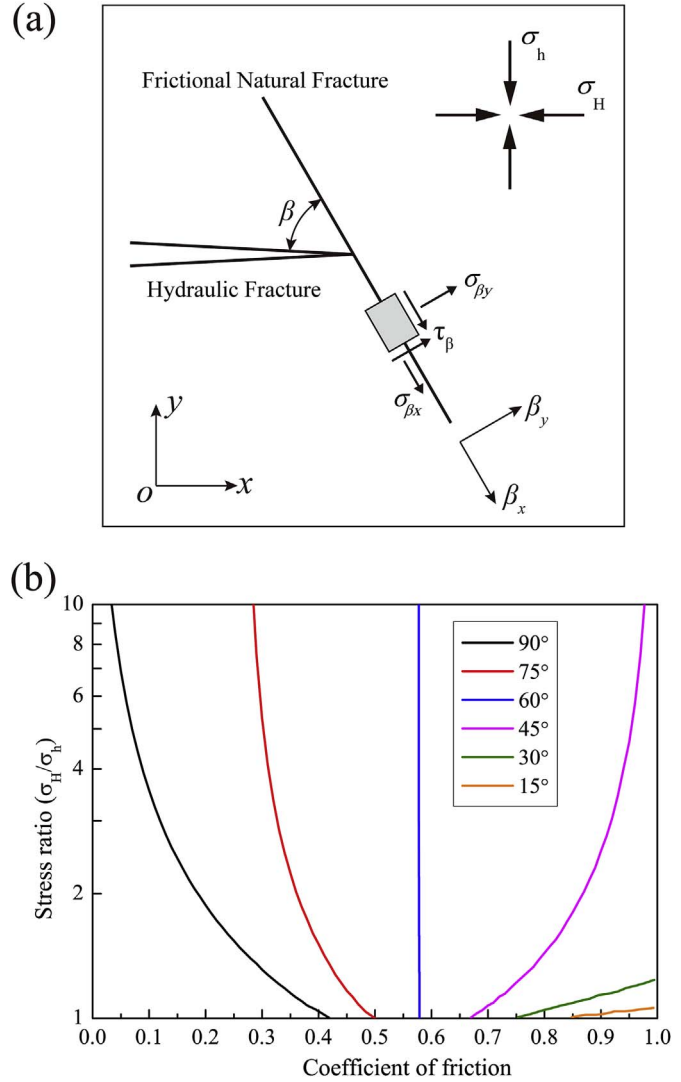


Fig. 3. (a) Schematic of a HF approaching a NF; (b) Plot of crossing criterion for several intersection angles between 0° and 90°.

HF and the frictional NF. This criterion assumes that the HF can cross the NF if the stress near the HF tip is able to prevent slip along the NF interfaces and the stress on the opposite side of the interfaces is adequate to reinitiate a new fracture. As shown in Fig. 3(a), a HF meets a frictional NF. The combined stress field around the HF tip is (Gu et al., 2011):

$$\begin{cases} \sigma_x = \sigma_H + \frac{K_I}{\sqrt{2\pi r}} \cos \frac{\theta}{2} \left(1 - \sin \frac{\theta}{2} \sin \frac{3\theta}{2} \right) \\ \sigma_y = \sigma_h + \frac{K_I}{\sqrt{2\pi r}} \cos \frac{\theta}{2} \left(1 + \sin \frac{\theta}{2} \sin \frac{3\theta}{2} \right) \\ \tau_{xy} = \frac{K_I}{\sqrt{2\pi r}} \sin \frac{\theta}{2} \cos \frac{\theta}{2} \cos \frac{3\theta}{2} \end{cases} \quad (5)$$

where σ_H and σ_h are the remote in-situ stresses; K_I is the stress intensity factor; (r, θ) represent the local polar coordinate system defined at the fracture tip. If the maximum principal stress σ_{\max} reaches the rock tensile strength T_0 and no slip along the interface occurs, a new fracture will initiate on the opposite side of the interface:

$$\begin{cases} \sigma_{\max} = T_0 \\ |\tau_\beta| < S_0 - \mu_f \sigma_{\beta y} \end{cases} \quad (6)$$

where $\sigma_{\beta y}$ and τ_β are the combined normal and shear stresses acting on the interface, respectively. S_0 is the cohesion of the interface and μ_f is the coefficient of friction. Fig. 3(b) shows the results obtained from this

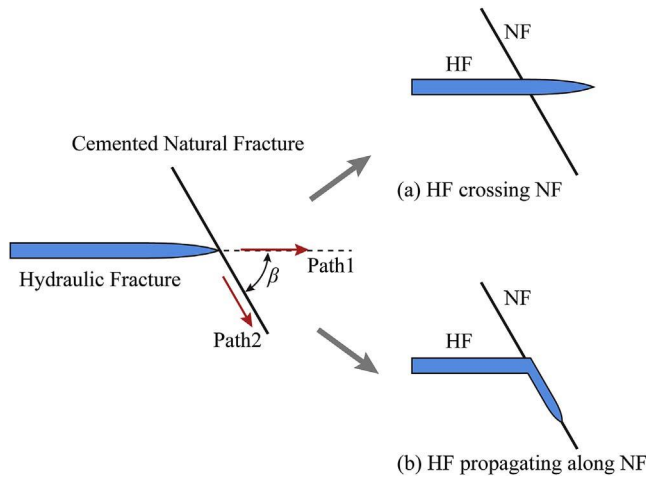


Fig. 4. Schematic of interaction process between a HF and a cemented NF.

criterion for several intersection angles, in the case when tensile strength $T_0 = 0$ and cohesion $S_0 = 0$. The domain at the left of each curve means the no crossing condition.

When a HF encounters a fully cemented NF, two scenarios of fracture propagation may occur (Dahi-Taleghani and Olson, 2011, 2014). In the first scenario (Fig. 4(a)), the HF may cross the NF and propagate along the direction of the maximum horizontal stress and the NF has no influence on the propagation of the HF. In the second scenario (Fig. 4(b)), the HF is arrested by the NF and diverts into it, forming an L-shaped fracture. Dahi-Taleghani and Olson (2011) demonstrated theoretically that the diversion for an oblique intersection will be in one direction only. However, if the toughness of the fracture cement depends strongly on the ratio of the Mode-I to the Mode-II stress intensity factors, a double branch could occur (He and Hutchinson, 1989). It should be noted that the cemented NF brought in our work is the same as that used in the work of Dahi-Taleghani and Olson, whose toughness is assumed to be independent of the ratio of the Mode-I to the Mode-II stress intensity factors, and no double branch will occur.

In this paper, a criterion on the basis of the energy release rate method is adopted to determine the cross/arrest behavior between the HF and the cemented NF (Dahi-Taleghani and Olson, 2011). The criterion assumes that the fracture will propagate in a direction along which the energy release rate is the maximum. The fracture starts to propagate if the maximum energy release rate is greater than or equal to the critical value G_c . The energy release rate in a specific orientation θ can be written as (Nuismer, 1975):

$$\begin{cases} G_\theta = \frac{K_{I\theta}^2 + K_{II\theta}^2}{E^*} \\ K_{I\theta} = \frac{1}{2} \cos\left(\frac{\theta}{2}\right) [K_I (1 + \cos \theta) - 3K_{II} \sin \theta] \\ K_{II\theta} = \frac{1}{2} \cos\left(\frac{\theta}{2}\right) [K_I \sin \theta + K_{II} (3 \cos \theta - 1)] \end{cases} \quad (7)$$

where θ is defined in the local polar coordinate system at the fracture tip; E^* is defined as E for plane stress and $E/(1-\nu^2)$ for plane strain (E is the Young's modulus and ν is the Poisson's ratio); K_I and K_{II} are the stress intensity factors for mode I and II, respectively. The cross/arrest behavior between the HF and the cemented NF is determined by magnitudes of the relative energy release rate G_m/G_c^{rock} and G_θ/G_c^{frac} . If G_m/G_c^{rock} is larger than G_θ/G_c^{frac} , namely G_θ/G_m is less than G_c^{frac}/G_c^{rock} , the HF will cross the NF, otherwise, the HF will deflect into the NF (G_m and G_θ represent the maximum energy release rate and the energy release rate in a specific orientation θ , respectively. G_c^{rock} represents the critical energy release rate of rock formation, and G_c^{frac} represents the energy required to open the unit area of the cement in the fracture or cement-matrix interface). The ratio G_θ/G_m comparing with the ratio G_c^{frac}/G_c^{rock} for pure mode I and II are shown in Fig. 5(a)

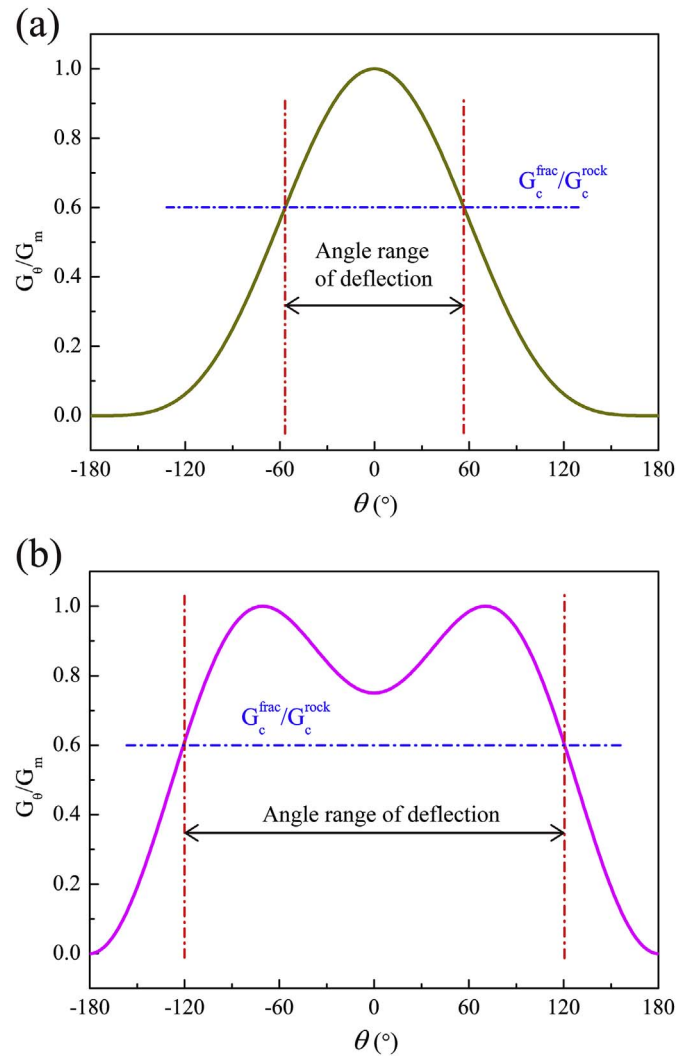


Fig. 5. The angle range of deflection (a) for pure mode I; (b) for pure mode II.

and (b), respectively. The HF will divert into the NF if the intersection angle β is between the two red dotted lines.

2.3. Fluid flow within the fractures

Fluid flow within the HF's can be given according to Poiseuille's law

$$q = -\frac{w^3}{12\mu} \frac{\partial p}{\partial s} \quad (8)$$

where q represents the fluid rate; w represents the fracture opening width; μ is the fluid viscosity; p is the fluid pressure imposed on the fracture surfaces. A one-dimensional curvilinear coordinate system (denoted by s) along the HF is defined, and the origin of the coordinate system is placed at the injection point. As the fluid is assumed to be incompressible and no fluid leak-off is considered in our model, the mass conservation equation should be satisfied according to the following equation:

$$\frac{\partial w}{\partial t} + \frac{\partial q}{\partial s} = 0 \quad (9)$$

Substituting Eq. (8) into Eq. (9) leads to the lubrication equation:

$$\frac{\partial w}{\partial t} - k \frac{\partial}{\partial s} \left(\frac{\partial p}{\partial s} \right) = 0 \quad (10)$$

where k can be considered as the permeability of the HF

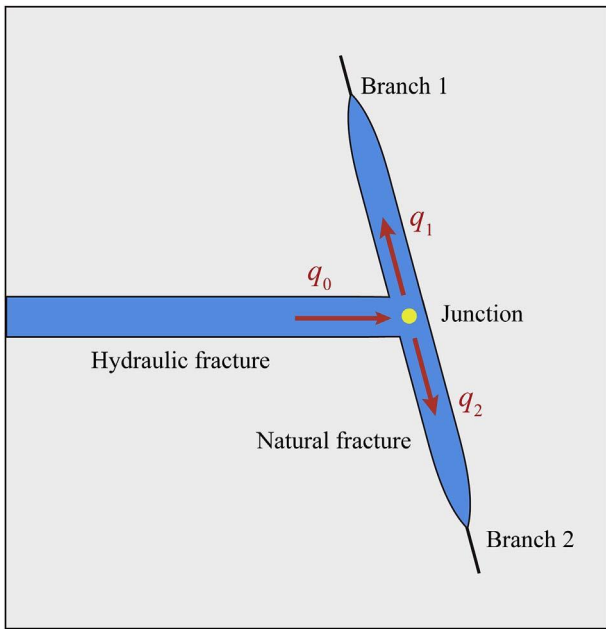


Fig. 6. Schematic of a T-shaped fluid-driven fracture.

$$k = \frac{w^3}{12\mu} \quad (11)$$

For a HF, Eq. (10) can be solved with the following initial and boundary conditions

$$\begin{cases} w(s, 0) = 0 \\ w(s_{tip}, t) = 0 \\ q(0, t) = Q_0 \\ q(s_{tip}, t) = 0 \end{cases} \quad (12)$$

as well as the global mass conservation equation

$$\int_0^{s_{tip}} w ds = \int_0^t Q_0 dt \quad (13)$$

where s_{tip} represents the location of the HF tip and Q_0 represents the injection rate of fluid at the injection point. For a T-shaped fluid-driven fracture formed after the intersection of a HF and a NF, as shown in Fig. 6, the same fluid pressure should be imposed at the junction for all branches, and flux into and out of the junction should be equal according to the law of conservation of mass. These boundary conditions at the junction can be automatically satisfied in our model by sharing a common fluid node (as shown in Fig. 7). More details will be shown later in Section 2.4.

2.4. The extended finite element method and discretization of governing equations

The XFEM is employed to approximate the displacement field \mathbf{u} to discretize the equilibrium equation. The XFEM allows the fracture to propagate along an arbitrary path without the requirement of remeshing and dramatically reduces the computational cost (Belytschko and Black, 1999; Budyn et al., 2004; Daux et al., 2000; Moes et al., 1999; Stolarska et al., 2001). In the XFEM, the displacement \mathbf{u} for any point \mathbf{x} in the domain Ω can be approximated as

$$\mathbf{u}(\mathbf{x}) = \sum_{I \in S_{all}} N_I^u(\mathbf{x}) \mathbf{u}_I + \sum_{I \in S_{frac}} N_I^u(\mathbf{x}) H(\mathbf{x}) \mathbf{a}_I + \sum_{I \in S_{tip}} N_I^u(\mathbf{x}) \sum_{l=1}^4 F_l(\mathbf{x}) \mathbf{b}_l^I + \sum_{I \in S_{junction}} N_I^u(\mathbf{x}) J(\mathbf{x}) \mathbf{c}_I \quad (14)$$

where S_{all} is the set of ordinary nodes, S_{frac} , S_{tip} , and $S_{junction}$ are the set

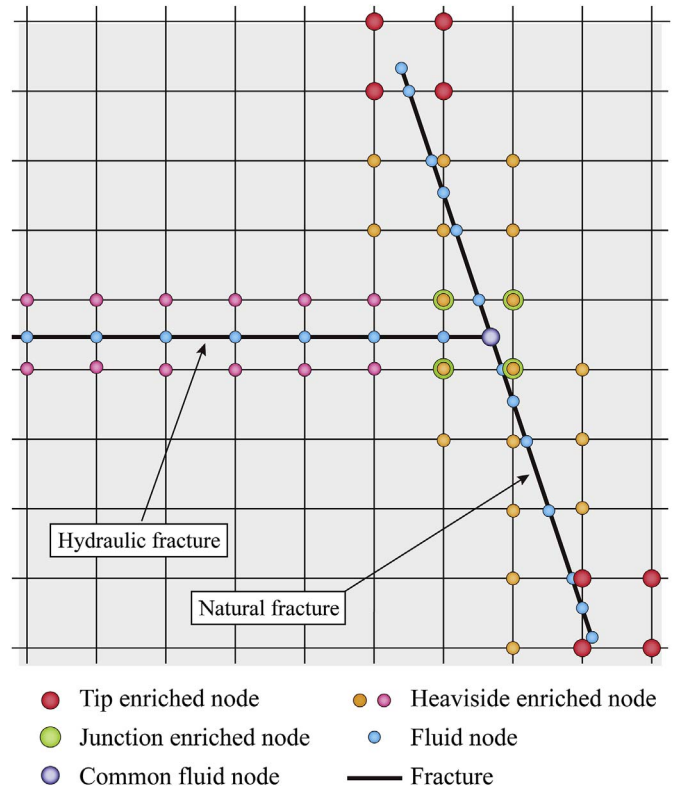


Fig. 7. Schematic of enriched nodes and fluid nodes of a T-shaped fracture.

of Heaviside enrichment nodes, the set of crack-tip enrichment nodes, and the set of junction enrichment nodes, respectively. \mathbf{u}_I represents the regular nodal degrees of freedom vector. \mathbf{a}_I , \mathbf{b}_l^I ($l = 1, 4$) and \mathbf{c}_I represent the enriched nodal degrees of freedom vectors. N_I^u is the standard finite element shape function of node I . $H(\mathbf{x})$ and $F_l(\mathbf{x})$ are the enrichment shape functions accounting for the displacement jump across fracture surfaces and the singular displacement field around the fracture tip, respectively.

$$H(\psi(x)) = \text{sign}(\psi(x)) = \begin{cases} +1, & \psi(x) > 0 \\ -1, & \psi(x) < 0 \end{cases} \quad (15)$$

$$\{F_l(r, \theta)\}_{l=1}^4 = \left\{ \sqrt{r} \sin \frac{\theta}{2}, \sqrt{r} \cos \frac{\theta}{2}, \sqrt{r} \sin \theta \sin \frac{\theta}{2}, \sqrt{r} \sin \theta \cos \frac{\theta}{2} \right\} \quad (16)$$

$J(\mathbf{x})$ is the junction enrichment shape functions accounting for the displacement field around the intersection point of two fractures. For a T-shaped junction, J equals 1, -1 or 0 on different subdomains created by the intersected fractures. Fig. 7 shows a typical enrichment strategy of two intersecting fractures. By substituting the approximation equation (Eq. (14)) into the weak form of the equilibrium equation, the discretized form of the equilibrium equation (more details can be found in Appendix A) can be obtained.

$$\mathbf{K}\mathbf{U} - \mathbf{Q}\mathbf{P} - \mathbf{F}^{ext} = \mathbf{0} \quad (17)$$

To approximate the one-dimensional pressure field $p(s, t)$ inside a HF, the fracture interface Γ_{HF} is discretized into fluid elements, as shown in Fig. 7. The pressure field can be approximated by the finite element method, that is

$$p(s) = \sum_{I \in S_{hf}} N_I^p(s) p_I \quad (18)$$

where S_{hf} is the set of fluid nodes; $N_I^p(s)$ represents the linear shape function of nodal pressure p_I for node I . By substituting Eq. (18) into the weak form of the lubrication equation, we can obtain the discretized

form of the fluid flow equation (details can be found in Appendix A), that is

$$\mathbf{Q}^T \Delta \mathbf{U} + \Delta t \mathbf{H} \mathbf{P} + \Delta t \mathbf{S} = \mathbf{0} \quad (19)$$

2.5. The fluid-solid coupling approach

The hydraulic fracturing model presented in this paper incorporates many physical processes such as deformation of rock formation, contact status between fracture surfaces, fractures initiation and propagation, interactions between HF and NFs, stress shadow effect and fluid flow within fractures. This highly nonlinear coupled system can be solved through the Newton-Raphson iterative method. As discussed above, the discretized form of the coupled equilibrium equation and fluid flow equation can be written as

$$\begin{cases} \mathbf{K} \mathbf{U} - \mathbf{Q} \mathbf{P} - \mathbf{F} = \mathbf{0} \\ \mathbf{Q}^T \Delta \mathbf{U} + \Delta t \mathbf{H} \mathbf{P} + \Delta t \mathbf{S} = \mathbf{0} \end{cases} \quad (20)$$

The coupled problem can be solved by three main steps during each time step. Step (i): determine the state of each fracture, that is, whether the HF is driven by fluid, and the contact status of each frictional NF, since the slip along the fracture interfaces may have an influence on the HF propagation. The Newton-Raphson iterative method based on the penalty method is adopted to solve the discretized nonlinear equilibrium equation (Eq. (17)) to determine the contact status (details can be found in Appendix B). Step (ii): the coupling between the deformation of HF and the fluid flow within fractures is also iteratively solved using the Newton-Raphson method (details can be found in Appendix B). Step (iii): the stress state of each fracture tip is calculated, and then the location of each fracture tip is updated according to the crack propagation criterion. Fig. 8 shows the flow chart of the coupled approach within each time step.

3. Results and discussion

3.1. Verification of the model

In this section, a corresponding numerical example is presented based on the experiment on Colton sandstone blocks in true triaxial stress condition at TerraTek laboratory (Gu et al., 2011) to verify the accuracy and efficiency of the proposed method. In order to simplify the calculation, we use a plane strain hydraulic fracturing model with uniform pressure imposed on the surfaces of HF, as shown in Fig. 9. The left edge of the computational domain is set as a symmetric boundary, and the width of the domain L_1 and L_2 are set as 0.2 m and 0.3 m, respectively. The initial HF is set in the middle of the left edge with a length of 0.05 m, and the NF is set in the middle of the model with a length of 0.2 m. The Young modulus E and Poisson's ratio ν of the sandstone are set to 20.4 GPa and 0.2, respectively. The tensile strength of the sandstone is set to 4.05 MPa. The coefficient of friction for the NF interfaces is set to 0.615 and the cohesion of the interfaces is assumed to be zero. The magnitude of the uniform pressure imposed on the HF surfaces is set as 15.17 MPa referring to the wellbore pressure. Other input parameters adopted in the example are shown in Table 1 (Gu et al., 2011).

The simulation is completed at the moment when the HF encounters the NF. The Von-Mises stress contours of the domain around the fractures with an intersection angle of 75° for two different groups of horizontal stress are shown in Fig. 10. When the maximum horizontal stress equals 17.24 MPa, the stress concentration appears at the domain around the HF tips (Fig. 10(a)), which means that no shear slip along the NF surfaces occurs. However, when the maximum horizontal stress is decreased to 8.27 MPa, the stress concentration appears at the domain around the NF (Fig. 10(b)), which means that the shear slip along the NF surfaces occurs. The comparisons of fracture sliding along the

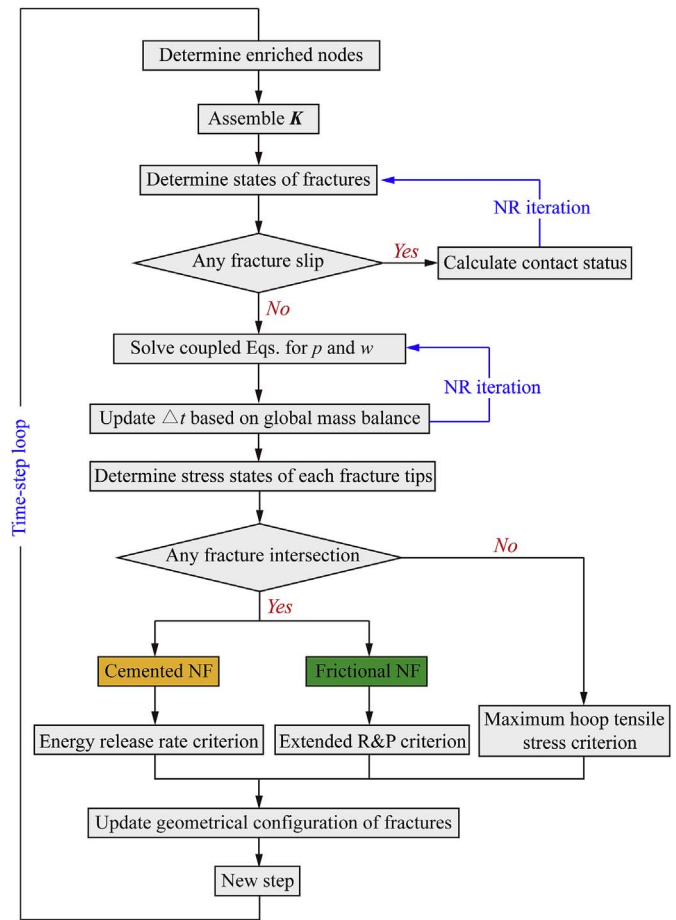


Fig. 8. Flow chart of the fluid-solid coupling approach.

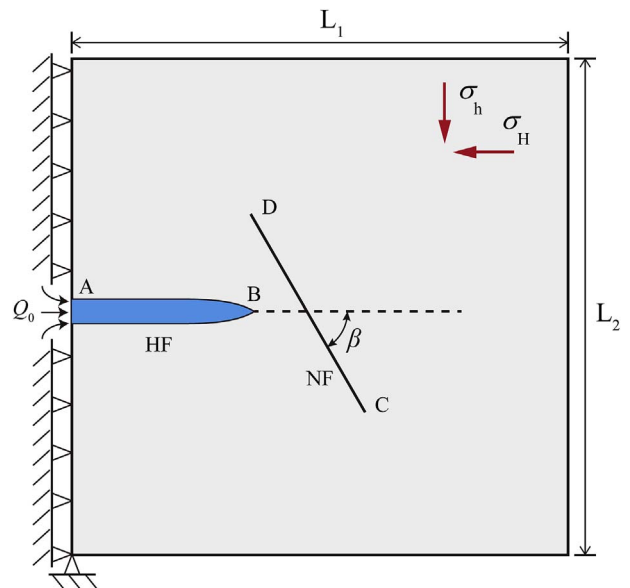


Fig. 9. The half symmetrical model for hydraulic fracturing.

NF for two groups of horizontal stress with different intersection angles are shown in Fig. 11(a). Based on the extended Renshaw and Pollard criterion, we can predict the behavior of cross/arrest according to the sliding along the NF surfaces. Fig. 11(b) shows the comparison results between numerical simulations and lab experiments, from which we can find that the numerical results are in excellent agreement with lab

Table 1
Input parameters for the validation model.

Intersection Angle	Maximum Horizontal Stress (MPa)	Minimum Horizontal Stress (MPa)	Crossing
90	13.79	6.89	Yes
90	7.58	6.89	No
75	17.24	6.89	Yes
75	8.27	6.89	No
45	17.24	6.89	No
45	8.27	6.89	No

experiments (Gu et al., 2011).

Through this numerical example, the accuracy of the contact model and the extended Renshaw and Pollard criterion for frictional NFs are validated. Moreover, the validation of the fluid-solid coupling approach for a KGD model has been presented in our previous work (Shi et al., 2016; Wang et al., 2016b), so it is not repeated here. The intersection of a fluid-driven fracture and a frictional NF and cemented NF will be studied in Sections 3.2 and 3.3, respectively.

3.2. A HF intersection with a frictional NF

In this section, a fully coupled hydraulic fracturing model is established in shale formation to study the process of the interaction between a HF and a frictional NF. The geometry of the model and the boundary condition are the same as those shown in Fig. 9. The width of the domain L_1 and L_2 are set as 30 m and 35 m, respectively. The initial HF is set in the middle of the left edge and is perpendicular to the edge with a length of 1 m. The frictional NF, whose middle point is set at (7.5 m, 17.5 m), has a length of 6 m and is aligned at an angle of β with respect to the initial HF direction. The in-situ stress is isotropic. Four intersection angles (90°, 75°, 60° and 45°) are investigated. Table 2 shows the input parameters.

The simulation is completed at the moment when the HF intersects with the NF. According to the extended Renshaw and Pollard criterion, the HF is arrested by the NF and propagates along it, forming a T-shaped fluid-driven fracture in the four cases (Fig. 12). Since the coalescence of fractures is a complex process, we suppose that the fluid fronts reach the tips of the NF as soon as the HF intersects with it. The maximum principal stress contours of the domain around the fractures with four different intersection angles are shown in Fig. 12. When the intersection angle is 90°, a tensile stress zone can be found in the vicinity of both tips of NF, and the stress distribution along the NF is symmetrical with respect to the intersection point (Fig. 12(a)). In addition, the fracture width and net pressure distribution along the NF are also symmetrical with respect to the intersection point (Fig. 13(a) and (b)). For the other three intersection angles, the stress distribution

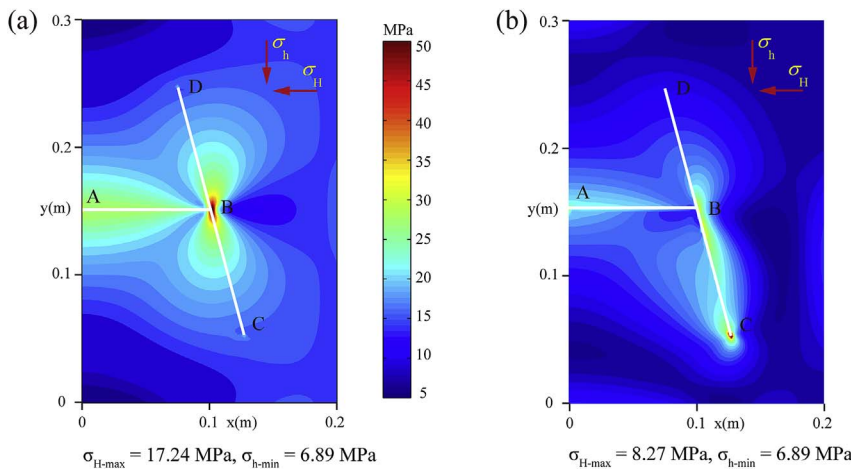


Fig. 10. Von-Mises stress contours of the domain around the fractures with an intersection angle of 75°.

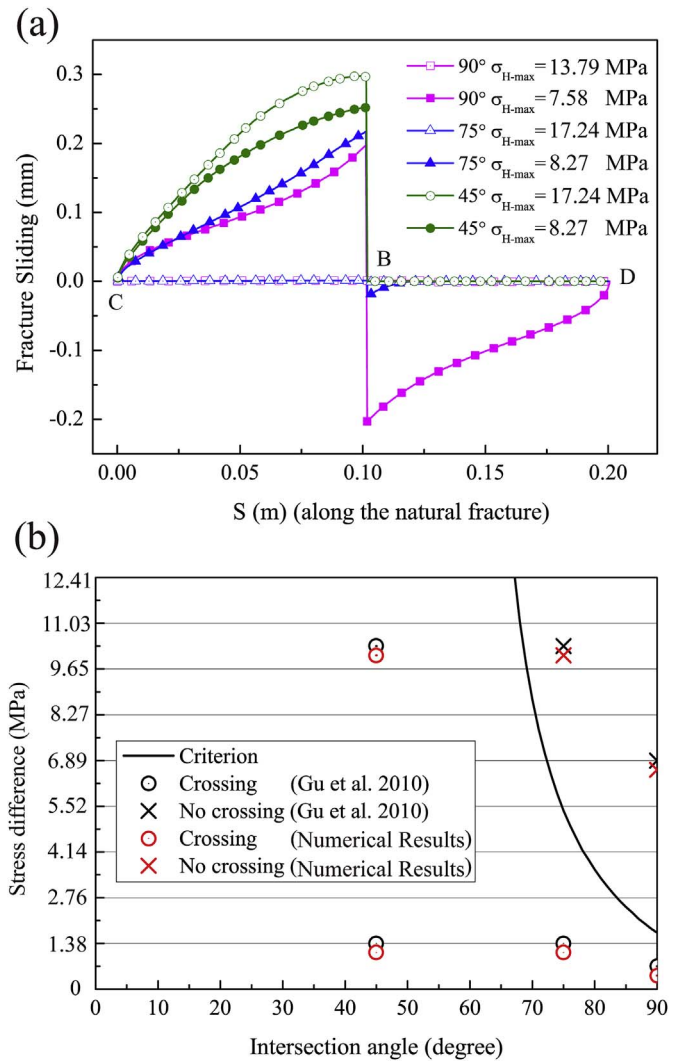


Fig. 11. (a) Fracture sliding along the NF; (b) Comparison results between numerical simulations and lab experiments.

along the NF becomes asymmetrical and the stress concentration is more significant in the vicinity of the lower tip of NF (Fig. 12(b), (c) and (d)). Meanwhile, the fracture width along the downward side of NF is larger than that along the upward side of NF. With the decrease of intersection angle, the fracture width along the downward side of NF increases while that along the upward side of NF decreases. When the

Table 2
Input parameters for the hydraulic fracturing model.

Input Parameter	Value
Young's modulus of rock, E	20 GPa
Poisson's ratio, ν	0.2
Friction coefficient of the NF, μ_f	0.3
Cohesion of the NF, S_0	0 MPa
Fracture toughness of the rock, K_{IC}	2 MPa m ^{1/2}
Tensile strength of the rock, T_0	1 MPa
Viscosity of fracturing fluid, μ	0.1 Pa s
Fluid pump rate, Q_0	0.001 m ² /s
Maximum horizontal stress, σ_{H-max}	5 MPa
Minimum horizontal stress, σ_{h-min}	5 MPa

intersection angle equals 45°, the downward side of NF has the largest width while the upward side of NF is nearly closed (Fig. 13(a)). No stress concentration occurs in the vicinity of the upper tip of NF (Fig. 12(d)). It denotes that under the combined action of the far-field stresses and the closure stress induced by the adjacent HF, a portion of the NF cannot be opened by the fluid pressure imposed on the fracture surfaces. The net pressure along the NF also becomes asymmetrical and decreases with the decrease of the intersection angle (Fig. 13(b)). It denotes that the resistance against fracture opening is less with a smaller intersection angle.

3.3. A HF intersection with a cemented NF

In order to compare the different interaction process between a HF and the two types of NF, a similar hydraulic fracturing model like that presented in Section 3.2 is established except that the frictional NF is

replaced by a cemented NF. The rock toughness K_{IC}^{rock} is 2 MPa m^{1/2} and the NF cement toughness K_{IC}^{frac} is 1.2 MPa m^{1/2}. The value of G_c^{frac}/G_c^{rock} equals 0.36. Other parameters are the same as those used in Section 3.2. The ratios of energy release rate G_θ/G_m for different intersection angles have been calculated at the moment when the HF encounters the cemented NF (using Eq. (7)). When the intersection angle equals 90°, the magnitude of G_θ/G_m equals 0.250, which is less than the value of G_c^{frac}/G_c^{rock} . According to the energy release rate criterion presented above, the HF can cross the NF and becomes a planar fracture (Fig. 14(a)). In this case the NF has no influence on the propagation of the HF. When the intersection angles equal 75°, 60° and 45°, the magnitudes of G_θ/G_m equal 0.396, 0.563 and 0.729, respectively. These values are all larger than the value of G_c^{frac}/G_c^{rock} . Hence, the HF is arrested by the NF and propagates along the downward side of the NF (Fig. 14(b), (c) and (d)), forming an L-shaped fluid-driven fracture. The upward side of NF stays closed and has no influence on the interaction process because the fracture interfaces are fully bonded by cement. The simulation is completed when the HF tip reaches the NF tip or propagates a half-length of the NF, as shown in Fig. 14. The stress concentration occurs at the near-tip region of HF (Fig. 14(a)) or in the vicinity of the lower tip of NF (Fig. 14(b), (c) and (d)). The fracture width and net pressure distribution along the diverted HF are shown in Fig. 15. An abrupt change can be seen in the fracture width at the intersection point when the HF diverts into the NF (Fig. 15(a)). The degree of fracture width change increases with the intersection angle (75°, 60° and 45°). However, larger abrupt change of fracture width at the intersection point makes it harder for the fluid to flow into the NF, which leads to a higher net pressure within the fracture (Fig. 15(b)). The pressure gradient also has a change at the intersection point for the no crossing cases. Moreover, the higher net pressure causes a larger fracture width for the diverted HF.

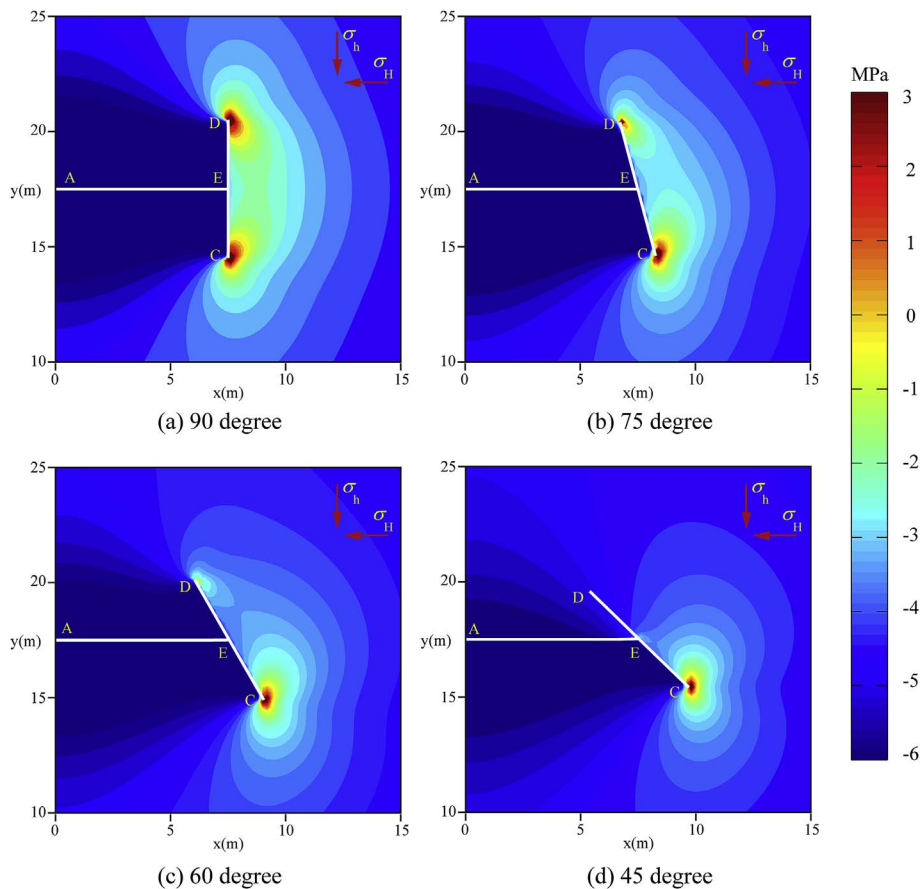


Fig. 12. The maximum principal stress contours of the domain around the fractures with four different intersection angles.

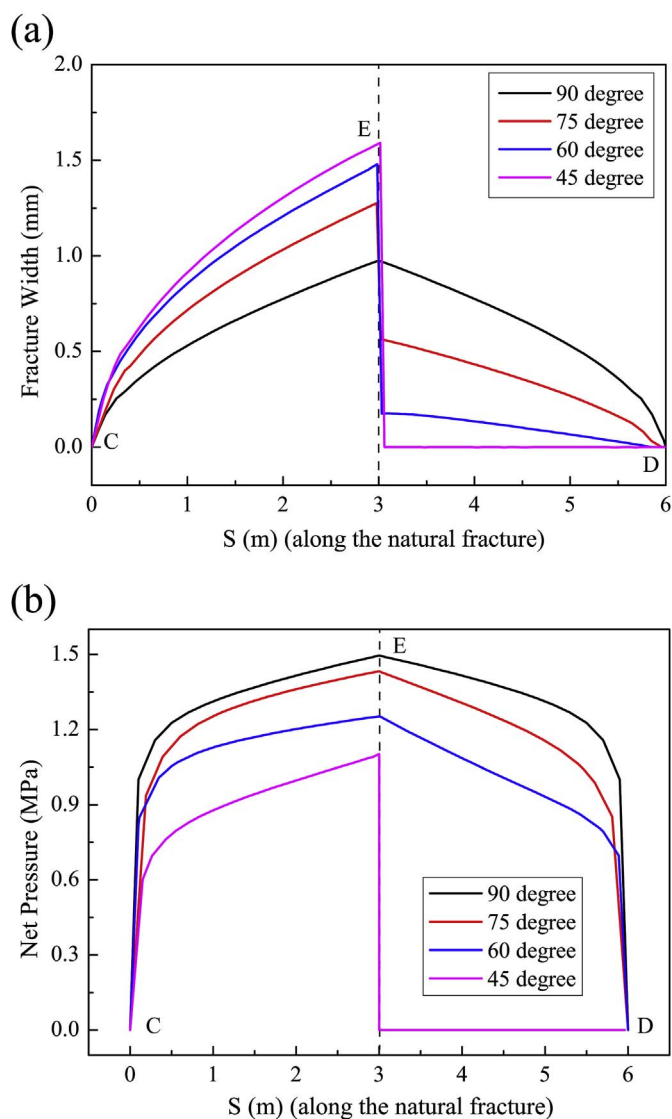


Fig. 13. (a) Fracture width distribution along the NF; (b) net pressure distribution along the NF.

3.4. Effects of the frictional NFs on the formation of fracture network

In this section, we conduct a series of hydraulic fracturing simulations in a shale formation that contains some specified frictional NFs to evaluate the effects of the frictional NFs on the formation of fracture network. The geometry of the model is shown in Fig. 16. The left edge of the computational domain is set as a symmetric boundary, and the width of the domain L_1 and L_2 are set as 60 m and 80 m, respectively. Five frictional NFs (marked as (1) to (5)) with the same length of 6 m are aligned at an angle of β with respect to the x-direction (Fig. 16). The middle point of NF(1) is set at (7.5 m, 40 m). The horizontal distance of NFs is set as $l_{1x} = l_{2x} = 4$ m, and the vertical distance of NFs is set as $l_{1y} = 4.5$ m and $l_{2y} = 9$ m, respectively. Other parameters for the simulation are shown in Table 3 unless otherwise noted. Since calculating the fluid flow within fracture network is a difficult problem, we assume that the uniform net pressure is imposed on the fracture surfaces for simplicity. This is equivalent to assuming a zero-viscosity fluid (Dahi-Taleghani and Olson, 2014; Olson and Taleghani, 2009). The fluid net pressure ($P - \sigma_{h-min}$) is assumed to be 2 MPa for the cases below.

In the first case, the value of angle β is set to 90° , and the friction coefficients of the five NFs are all set as 0.3. The in-situ stress is isotropic. The maximum principal stress contours of the domain around

the fractures and fracture opening distributions at the last step are presented in Fig. 17(a) and (b), respectively. The results show that the initial HF intersects with NF(1) first and no crossing occurs. Due to the symmetry of the model, the HF diverts into both the upward and downward sides of NF(1), and keeps propagating until reaches the tip. Afterwards, the two tips of NF(1) synchronously grow and turn to the direction perpendicular to the minimum principal stress. Then the branch growing from the upper tip of NF(1) intersects with NF(3) and the branch growing from the lower tip of NF(1) intersects with NF(2). The closure stress induced by the adjacent hydro-fractures, which is called as the stress shadow effect, makes the upward side of NF(2) and downward side of NF(3) close. Under the combined action of the far-field stresses and the natural-hydraulic fracture interaction, the upper tip of NF(2) and the lower tip of NF(3) stop growing while the lower tip of NF(2) and the upper tip of NF(3) continue to propagate and intersect with NF(4) and NF(5), respectively. The upward side of NF(4) and the downward side of NF(5) also stay closed because of the stress shadow effect. Only the lower tip of NF(4) and the upper tip of NF(5) continue to propagate in the formation, resulting in symmetrical distribution of propagation paths, as well as stress and fracture opening (Fig. 17(a) and (b)). It should be remarked that the fracture openings of the NFs are smaller compared with that of the HF in formation. This is because of the unfavorable orientation of the NFs and the effect of stress shadow. The abrupt change in fracture width at the intersection point makes the fluid flow and proppants transport within fracture network harder, likely to cause a sand plug.

In the second and third cases, the values of angle β are set to 75° and 45° , respectively, in order to investigate the effects of intersection angle on the formation of fracture network. Other parameters are the same as those used in the first case. As shown in Fig. 18, when the angle β equals 75° , the configuration of the fracture network created at last is similar with that in the first case, except that the fracture propagation paths are asymmetrical. However, when the angle β decreases to 45° , the creation of the fracture network is different. After the initial HF intersects with NF(1), only the lower tip of NF(1) continues to propagate while the upper tip of NF(1) stops growing under the influence of stress shadow. At last, the fracture network created in this case is simpler compared with the first and second cases.

In order to investigate the effects of friction coefficient and tensile strength of rock on the formation of fracture network, the fourth and fifth cases are carried out. The values of tensile strength T_0 are set to 1 MPa and 5 MPa for the fourth and fifth cases, respectively. The values of friction coefficient are set as 0.3 for NF(1) and 0.8 for the other four NFs (NF(2), NF(3), NF(4) and NF(5)) in the two cases. Other parameters are the same as those used in the second case. As shown in Fig. 19, in the fourth case, the branch growing from the upper tip of NF(1) crosses NF(3) and NF(5), due to their larger friction coefficients. The branch growing from the lower tip of NF(1) is arrested by NF(2) and NF(4) even if their friction coefficients are equal to 0.8 as well. This can be explained that their intersection angles are smaller. In the fifth case, when the tensile strength T_0 increases to 5 MPa, the branches growing from both the upper and lower tips of NF(1) cannot cross the NFs, even if their friction coefficients are the same as those in the fourth case. The last configuration of the fracture network formed in the fifth case is similar with that in the second case, as shown in Fig. 18(a) and Fig. 19(b).

In order to investigate the effects of in-situ stress difference on the creation of fracture network, the maximum and minimum horizontal stresses are set to -10 MPa and -5 MPa, respectively. The fluid net pressure ($P - \sigma_{H-max}$) is assumed to be 2 MPa. In the sixth case, other parameters are the same as those used in the second case. As shown in Fig. 20(a), the initial HF intersects with NF(1) and is arrested by it. Under the combined action of the far-field stresses and the natural-hydraulic fracture interaction, the upper tip of NF(1) stops growing while the lower tip of NF(1) continues to propagate and intersects with NF(2). However, it cannot cross NF(2) and is arrested by it. Then both

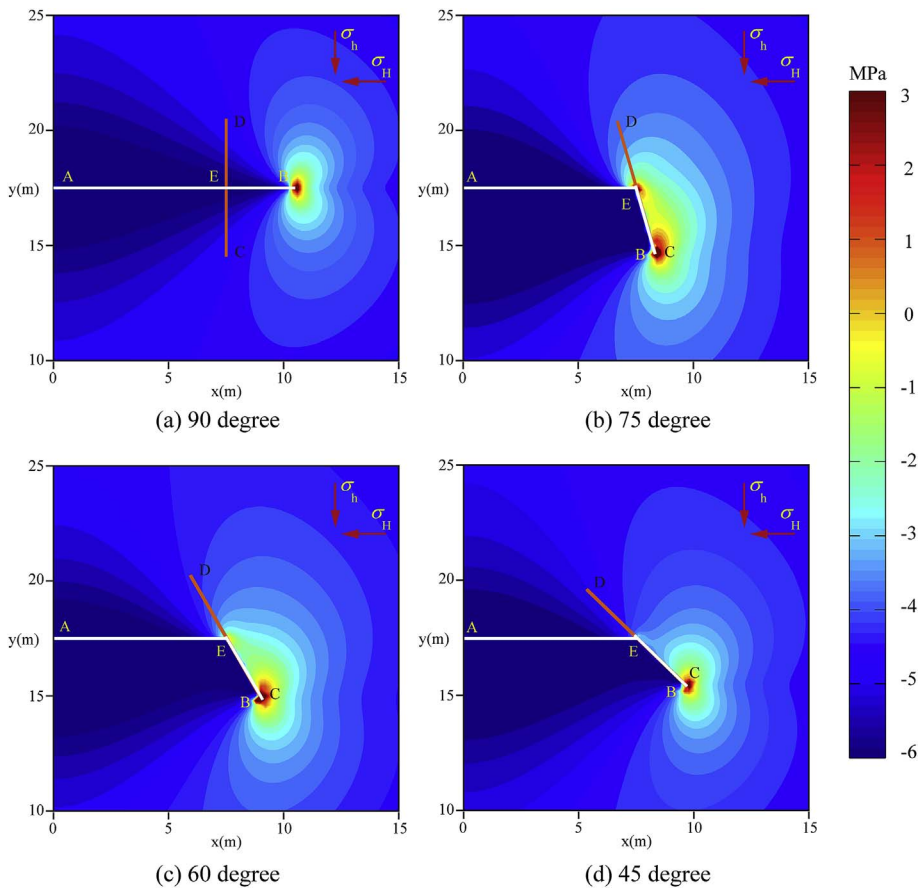


Fig. 14. The maximum principal stress contours of the domain around the fractures with four different intersection angles.

the upper and lower tips of NF(2) continue to grow. The branch growing from the lower tip of NF(2) intersects with NF(4) and is arrested by it. Then both the upper and lower tips of NF(4) continue to grow. The last configuration of the fracture network formed in the sixth case is different from that in the second case (Fig. 18(a) and Fig. 20(a)). In the seventh case, other parameters are the same as those used in the fourth case. As shown in Fig. 20(b), the branch growing from the lower tip of NF(1) crosses NF(2) and continues to propagate in the formation because of the larger friction coefficient of NF(2). The last configuration of the fracture network formed in the seventh case is simpler in comparison to that in the fourth case (Fig. 19(a) and Fig. 20(b)).

From the above, we find that the complexity of the fracture network created in the formation containing several frictional NFs mainly depends on the in-situ stress difference, friction coefficient of NFs, intersection angle and tensile strength of rock. Larger stress difference, friction coefficient and intersection angle and smaller tensile strength of rock often make the HF cross the NFs. Conversely, smaller stress difference and friction coefficient and larger tensile strength of rock often make the HF arrested by the NFs and lead to the creation of a more complex fracture network. Besides, with a smaller intersection angle, the stress shadow effect may lead to the partial closure of NFs.

3.5. Effects of the cemented NFs on the formation of fracture network

In this section, we conduct a series of hydraulic fracturing simulations in a shale formation that contains some specified cemented NFs to evaluate the effects of the cemented NFs on the formation of fracture network. The geometrical model is the same as that in Section 3.4 except that the frictional NFs are replaced by the cemented NFs. The value of angle β is set to 75° . The ratios G_c^{frac}/G_c^{rock} for the five cemented NFs are marked as R_1 , R_2 , R_3 , R_4 and R_5 , respectively.

In the first case, the values of R_{1-5} are all set to 0.3 for the five

cemented NFs. Other parameters are the same as those shown in Table 3. The maximum principal stress contours of the domain around the fractures and the fracture opening distribution along the fractures are presented in Fig. 21(a) and (b), respectively. The initial HF intersects with NF(1) first and is arrested by it. Then, the HF diverts into the downward side of NF(1) until reaches the lower tip of NF(1). The upward side of NF(1) stays closed and has no influence on the interaction process because the fracture interfaces are fully bonded by cement. This result is different from that shown in Section 3.4 (Fig. 18(a)), since a HF intersection with a cemented NF is most likely to form an L-shaped fracture while a HF intersection with a frictional NF is most likely to form a T-shaped fracture. The branch growing from the lower tip of NF(1) continues to propagate and intersects with NF(2). After that, a similar interaction process is repeated, and the branch growing from the lower tip of NF(2) continues to propagate and intersects with NF(4). The configuration of fracture network formed at last is shown in Fig. 21(a), from which we can find that the fracture network is simpler in comparison to the result shown in Fig. 18(a). Besides, it should be remarked that the fracture openings of NFs are also smaller compared with that of HF in rock formation. This is because of the unfavorable orientation of the NFs and the effects of stress shadow.

In the second case, the values of R_2 and R_3 are set to 0.6 and the values of R_4 and R_5 are set to 0.8, respectively. Other parameters are the same as those used in the first case. The interaction process between the initial HF and NF(1) is similar with that in the first case. However, the branch growing from the lower tip of NF(1) crosses NF(2) due to the larger ratio R_2 . After crossing, the fracture continues to grow in the rock formation and a simpler fracture network is created at last (Fig. 22(a)). In the third case, all the parameters are the same as those used in the second case except that the value of angle β is set to 45° . The branch growing from the lower tip of NF(1) is arrested by NF(2) and diverts into the downward side of NF(2) because of the smaller intersection

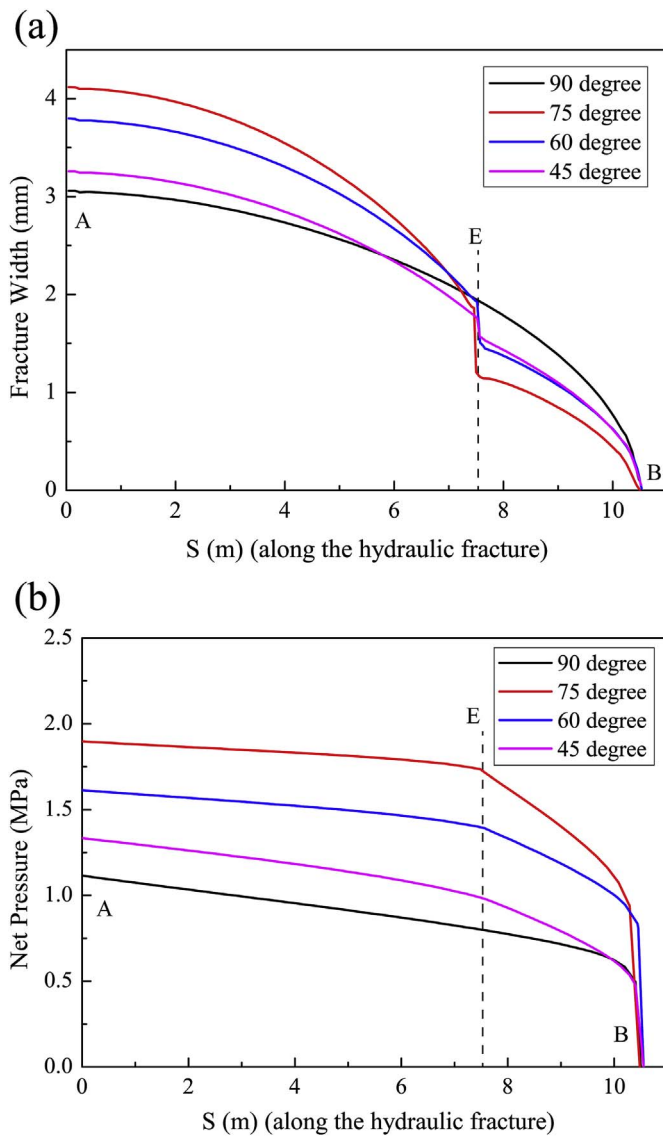


Fig. 15. (a) Fracture width distribution along the diverted HF; (b) net pressure distribution along the diverted HF.

angle. The branch growing from the lower tip of NF(2) still crosses NF(4), even if the intersection angle is smaller (Fig. 22(b)). This can be explained that the ratio R_4 is larger than ratio R_2 .

In order to investigate the effects of in-situ stress difference on the formation of fracture network. The maximum and minimum horizontal stresses are set to -10 MPa and -5 MPa, respectively, for the fourth and fifth cases. The fluid net pressure ($P-\sigma_{H-max}$) is assumed to be 2 MPa. In the fourth and fifth cases, other parameters are the same as those used in the second and third cases, respectively. The last configurations of fracture network (Fig. 23(a) and (b)) are similar with those shown in the second and third cases (Fig. 22(a) and (b)), respectively. It denotes that the stress difference has nearly no effect on the interaction process of a HF and a cemented NF. However, in the formation containing plenty of cemented NFs, the stress difference still has an influence on the formation of fracture network (Dahi-Taleghani and Olson, 2014), since the propagation paths of fractures in rock formation are affected by the stress difference.

From the above discussion, we find that the complexity of the fracture network created in the formation containing several cemented NFs mainly depends on the intersection angle, cement toughness of NFs and rock fracture toughness. Smaller intersection angle and cement toughness of NFs and larger rock fracture toughness often lead to more

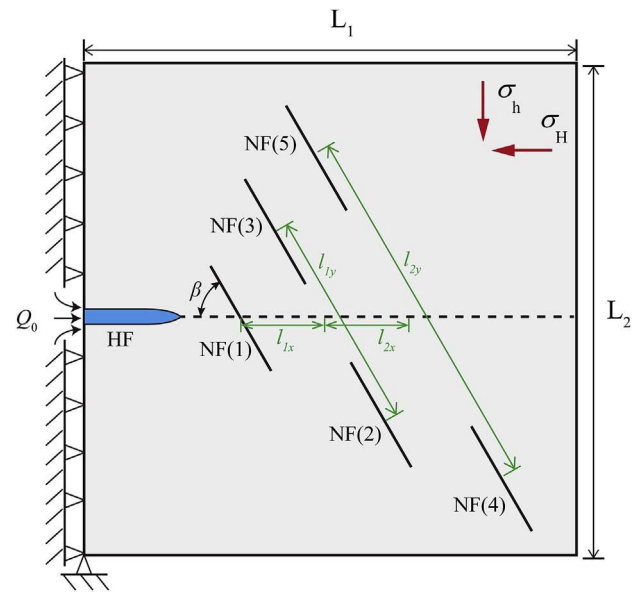


Fig. 16. Illustration of the fracture geometries where the solid lines represent pre-existing NFs marked as (1) to (5).

Table 3
Input parameters for the fracture network model.

Input Parameter	Value
Young's modulus of rock, E	20 GPa
Poisson's ratio, ν	0.2
Friction coefficient of the NF, μ_f	0.3
Cohesion of the NF, S_0	0 MPa
Fracture toughness of the rock, K_{IC}	2 MPa m ^{1/2}
Tensile strength of the rock, T_0	1 MPa
Uniform net pressure, ($P-\sigma_{h-min}$)	2 MPa
Maximum horizontal stress, σ_{H-max}	5 MPa
Minimum horizontal stress, σ_{h-min}	5 MPa

complex fracture network. The in-situ stress difference has nearly no influence on the interaction process of a HF and a cemented NF. Moreover, for the same initial geometrical configuration of NFs, hydraulic fracturing often leads to more complex fracture network in the formation containing frictional NFs in comparison to the formation containing cemented NFs.

4. Conclusions

In this study, we established a 2D fully coupled XFEM-based hydraulic fracturing model in which the interaction of HF and NFs, stress shadow effect, fluid flow within fractures, contact conditions of fractures and development process of fracture network are all considered. The effects of the frictional and cemented NFs on the HF propagation and the creation of fracture network are compared. The following conclusions can be drawn from this study:

- (1) When the HF intersects with the frictional NFs, the cross/arrest behavior mainly depends on the intersection angle, stress difference, friction coefficient of NFs, as well as rock tensile strength. Smaller stress difference, smaller friction coefficient, and larger tensile strength of rock often make the HF arrested by NFs, leading to more complex fracture network.
- (2) When the HF intersects with the cemented NFs, the cross/arrest behavior mainly depends on the intersection angle, cement toughness of NFs and rock fracture toughness. Smaller intersection angle, smaller cement toughness of NF, and larger rock fracture toughness often lead to more complex fracture network.

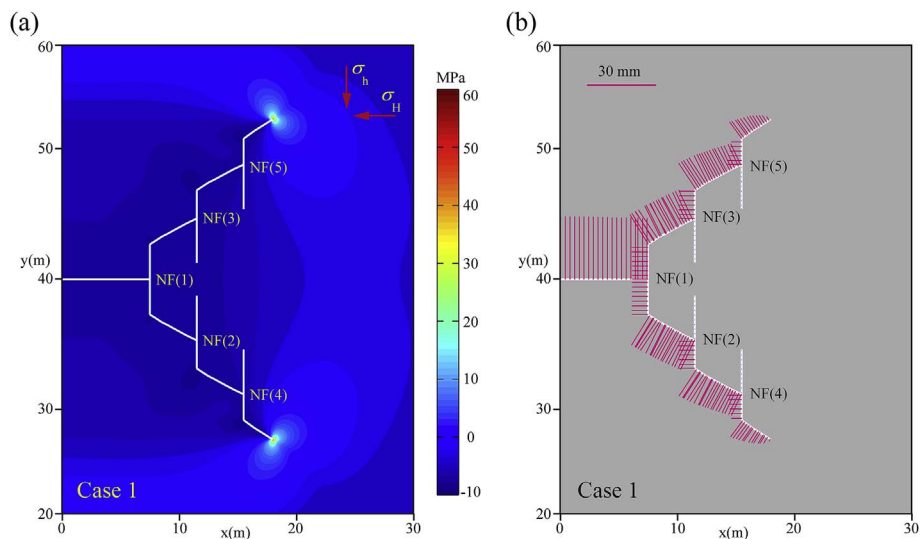


Fig. 17. (a) The maximum principal stress contours of the domain around the fractures; (b) the fracture opening distribution along the fractures.

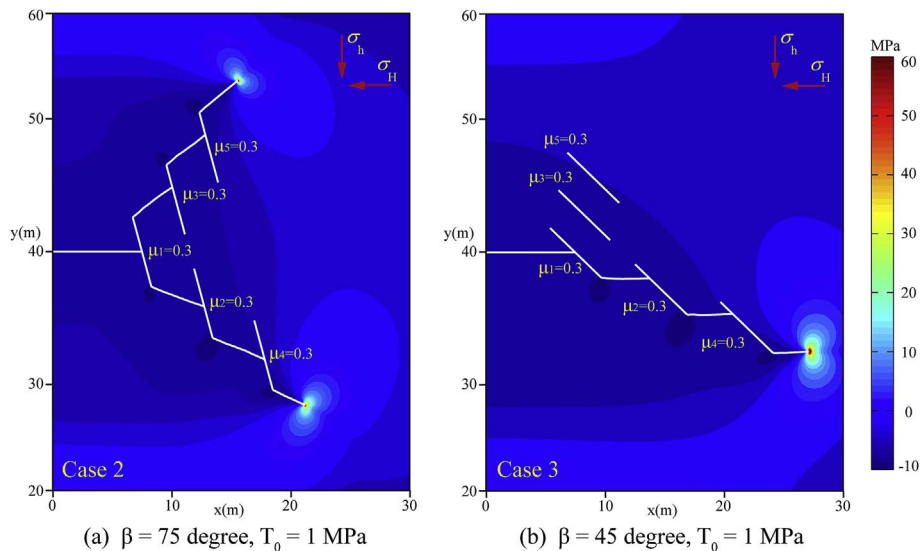


Fig. 18. The maximum principal stress contours of the domain around the fractures for two different oblique angles (a) β = 75°; (b) β = 45°.

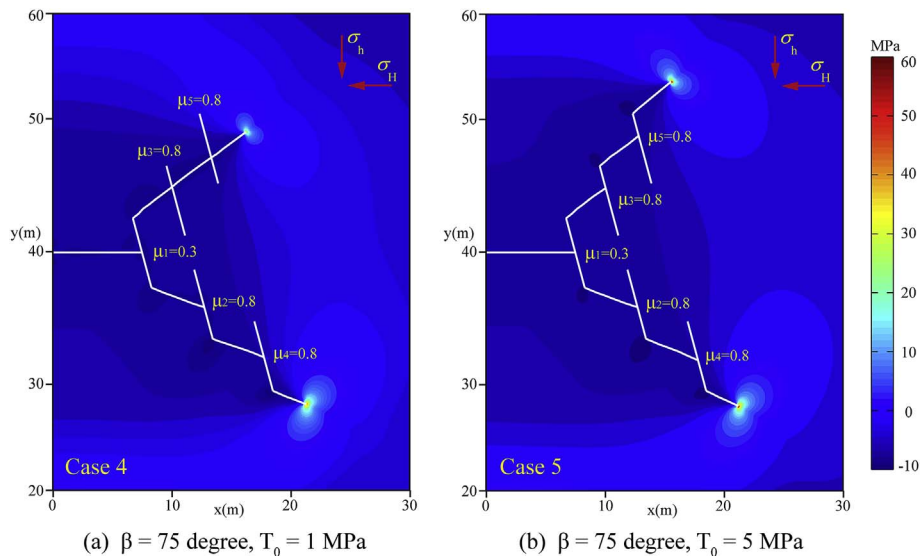


Fig. 19. The maximum principal stress contours of the domain around the fractures for two different tensile strengths (a) T₀ = 1 MPa; (b) T₀ = 5 MPa.

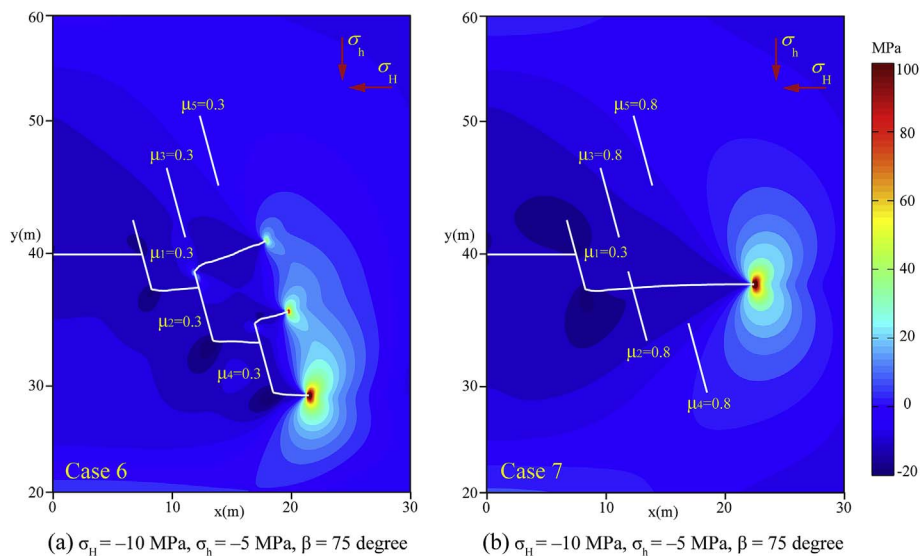


Fig. 20. The maximum principal stress contours of the domain around the fractures for a stress difference of 5 MPa.

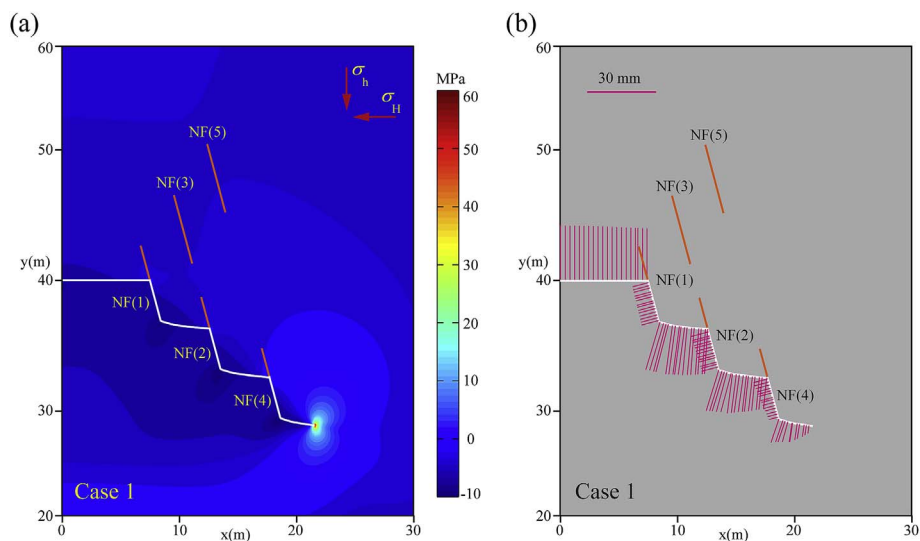


Fig. 21. (a) The maximum principal stress contours of the domain around the fractures; (b) the fracture opening distribution along the fractures.

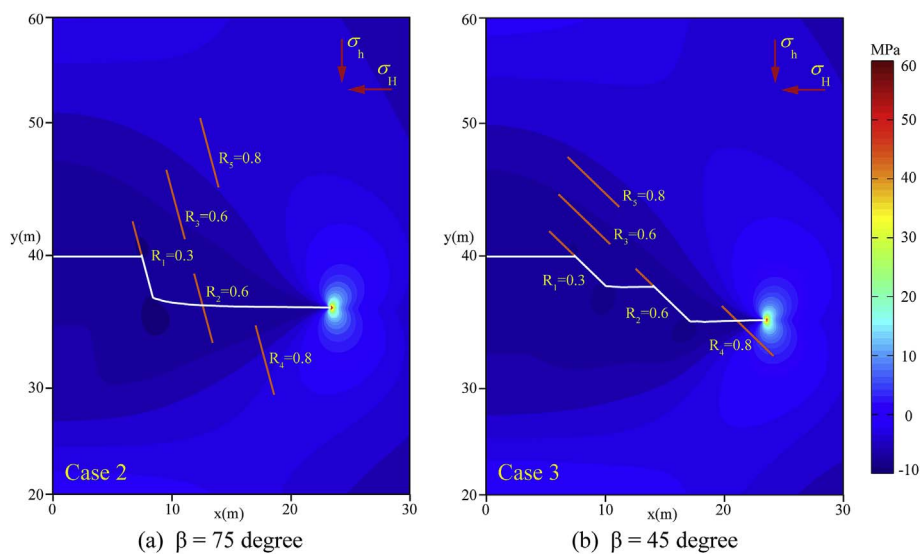


Fig. 22. The maximum principal stress contours of the domain around the fractures for two different oblique angles (a) $\beta = 75^\circ$; (b) $\beta = 45^\circ$.

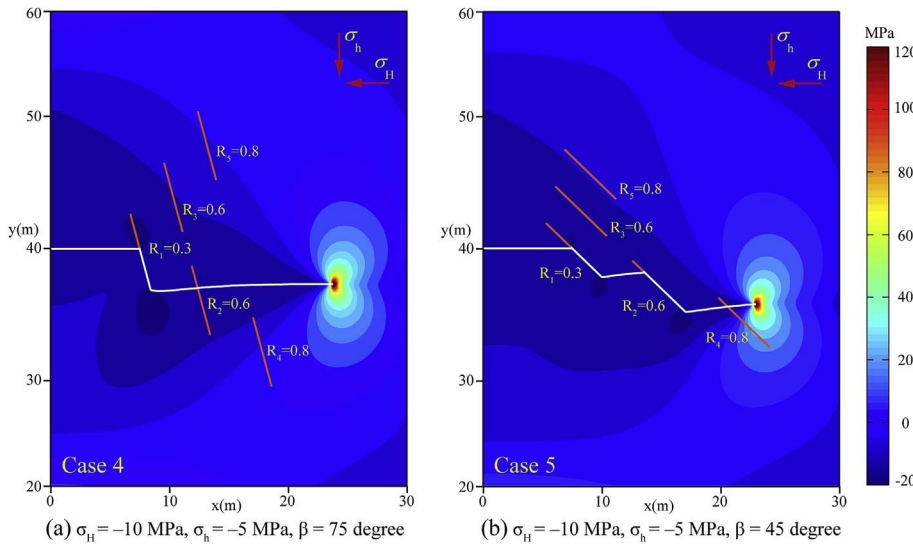


Fig. 23. The maximum principal stress contours of the domain around the fractures with stress difference equaling to 5 MPa.

(3) When a HF intersects with a NF and is arrested by the NF, it is most likely to form an L-shaped fracture for cemented NF and form a T-shaped fracture for frictional NF. For this reason, without considering the un-propped fractures induced by the stress shadowing effect, hydraulic fracturing often leads to more complex fracture network in the formation containing frictional NFs in comparison to the formation containing cemented NFs with the same initial geometrical configuration of NFs.

The numerical model presented in this study can be adopted to estimate the intersection behavior between HF and NFs and the

formation of fracture network in shale formations containing a large number of pre-existing fractures. Furthermore, the simulation results can serve as a guide for the optimum design of hydraulic fracturing to enhance production.

Acknowledgement

This work was jointly supported by the National Natural Science Foundation of China (11472263, 11525211), the CNPC-CAS Strategic Cooperation Research Program (2015A-4812) and the Natural Science Foundation of Jiangsu Province (BK20170457).

Appendix A. Discretization of equilibrium and fluid flow equations

The equilibrium equation (Eq. (1)) can be written in the weak form, that is

$$\int_{\Omega} \delta \epsilon : \sigma d\Omega + \int_{\Gamma_{HF}} [[\delta \mathbf{u}]] \cdot \mathbf{p} \mathbf{n}_{\Gamma_{HF}} d\Gamma + \int_{\Gamma_{NF}} [[\delta \mathbf{u}]] \cdot \mathbf{t}^{cont} d\Gamma = \int_{\Gamma} \delta \mathbf{u} \cdot \mathbf{t} d\Gamma \tag{A1}$$

where $\mathbf{u}(\mathbf{x}, t)$ is the trial function and $\delta \mathbf{u}(\mathbf{x}, t)$ is the test function for the displacement field; $[[\mathbf{u}]]$ represents the displacement jump across the interfaces of fractures.

The lubrication equation (Eq. (10)) can be given in the weak form, that is

$$\int_{\Gamma_{HF}} \left(\delta p \frac{\partial w}{\partial t} + \frac{\partial(\delta p)}{\partial s} k \frac{\partial p}{\partial s} \right) d\Gamma - \delta p \Big|_{s=0} Q_0 = 0 \tag{A2}$$

where $\delta p(s, t)$ is the test function.

The pressure field can be approximated by the finite element method:

$$p(s) = \sum_{I \in S_{hf}} N_I^p(s) p_I \equiv \mathbf{N}^p(s) \mathbf{P} \tag{A3}$$

where $\mathbf{N}^p(s)$ is the matrix of shape function and \mathbf{P} is the nodal pressure vector.

The fracture opening displacement vector \mathbf{w} can be approximated by

$$\mathbf{w} = \sum_{I \in S_w} N_I^w \mathbf{u}_I \equiv \mathbf{N}^w \mathbf{U} \tag{A4}$$

where \mathbf{N}^w is the matrix of shape function that transfers the nodal displacement to fracture width and \mathbf{U} is the vector of global nodal displacement.

By substituting the displacement and pressure approximations (Eqs. (14), (A3) and (A4)) into the weak form of the equilibrium equation (Eq. (A1)) and the lubrication equation (Eq. (A2)), the discretized form of the coupling equations can be written as

$$\mathbf{K} \mathbf{U} - \mathbf{Q} \mathbf{P} - \mathbf{F}^{ext} = \mathbf{0} \tag{A5}$$

$$\mathbf{Q}^T \Delta \mathbf{U} + \Delta t \mathbf{H} \mathbf{P} + \Delta t \mathbf{S} = \mathbf{0} \tag{A6}$$

In Eq. (A5), the global nodal displacement vector \mathbf{U} can be divided into two parts: \mathbf{U}_s (all the standard DOFs) and \mathbf{U}_e (all the enriched DOFs). The calculation of fracture width is only related to the part \mathbf{U}_e . Then, the global stiffness matrix \mathbf{K} can be divided into four parts based on the division of \mathbf{U}

$$\mathbf{K} = \begin{bmatrix} \int_{\Omega} (\mathbf{B}^{std})^T \mathbf{D} \mathbf{B}^{std} d\Omega & \int_{\Omega} (\mathbf{B}^{std})^T \mathbf{D} \mathbf{B}^{enr} d\Omega \\ \int_{\Omega} (\mathbf{B}^{enr})^T \mathbf{D} \mathbf{B}^{std} d\Omega & \int_{\Omega} (\mathbf{B}^{enr})^T \mathbf{D} \mathbf{B}^{enr} d\Omega + \int_{\Gamma_{NF}} (\mathbf{N}^w)^T \mathbf{D}^{cont} \mathbf{N}^w d\Gamma \end{bmatrix}$$

$$\equiv \begin{bmatrix} \mathbf{K}_{ss} & \mathbf{K}_{se} \\ \mathbf{K}_{es} & \mathbf{K}_{ee} + \mathbf{K}_{ee}^{cont} \end{bmatrix}$$
(A7)

where \mathbf{D}^{cont} is the contact stiffness of fracture interfaces. The coupling matrix \mathbf{Q} and the external loading vector \mathbf{F}^{ext} are defined as

$$\mathbf{Q} = \int_{\Omega} (\mathbf{N}^w)^T \mathbf{n}_{\Gamma_{HF}} \mathbf{N}^p d\Omega$$
(A8)

$$\mathbf{F}^{ext} = \int_{\Gamma_i} (\mathbf{N}^u)^T \mathbf{t} d\Gamma$$
(A9)

In Eq. (A6), Δt is the time increment. The flow matrix \mathbf{H} and the source term \mathbf{S} are defined as

$$\mathbf{H} = \int_{\Gamma_{HF}} k \left(\frac{\partial \mathbf{N}^p}{\partial s} \right)^T \frac{\partial \mathbf{N}^p}{\partial s} ds$$
(A10)

$$\mathbf{S} = \mathbf{N}^p(s)^T|_{s=0} Q_0$$
(A11)

Appendix B. Newton-Raphson method for contact iteration and fluid-solid coupling iteration

The discretized equilibrium equation (Eq. (A5)) is not linear when considering the frictional interaction between fracture surfaces, since the global stiffness matrix \mathbf{K} consists of a contact stiffness matrix \mathbf{K}_{ee}^{cont} that incorporates the unknown contact condition related to displacement \mathbf{U} . Therefore, Eq. (A5) can be iteratively solved using Newton-Raphson method based on the penalty method to predict the slip condition along fractures. The residual vector $\hat{\mathbf{R}}^i$ and the associated Jacobian matrix $\hat{\mathbf{J}}^i$ for the equilibrium equation at the contact iteration step i can be written as

$$\hat{\mathbf{R}}^i = \mathbf{K}^i \mathbf{U}^i - \mathbf{Q} \mathbf{P} - \mathbf{F}^{ext}$$
(B1)

$$\hat{\mathbf{J}}^i = \mathbf{K}^i$$
(B2)

Thus, the displacement \mathbf{U} can be updated at each iteration by

$$\mathbf{U}^{i+1} = \mathbf{U}^i - \frac{\hat{\mathbf{R}}^i}{\hat{\mathbf{J}}^i}$$
(B3)

The convergence criterion for the contact iteration can be written as

$$\eta_c = \|\hat{\mathbf{R}}^i\| / \|\hat{\mathbf{R}}^0\| \leq \varepsilon_{tol}^c$$
(B4)

where $\hat{\mathbf{R}}^i$ and $\hat{\mathbf{R}}^0$ are the residual vector at the i th and initial iteration steps, respectively. The tolerance ε_{tol}^c is taken as 10^{-3} in this paper.

The Newton-Raphson iterative algorithm is also used to solve the coupled equations (Eqs. (A5) and (A6)) at each time step. The residual vector \mathbf{R}^n and the associated Jacobian matrix \mathbf{J}^n for the coupled equations at the iteration step n can be written as

$$\mathbf{R}^n = \begin{bmatrix} \mathbf{0} & \mathbf{0} \\ -\mathbf{Q}^T & \mathbf{0} \end{bmatrix} \begin{bmatrix} \Delta \mathbf{U} \\ \Delta \mathbf{P} \end{bmatrix}^n + \begin{bmatrix} \mathbf{K} & -\mathbf{Q} \\ \mathbf{0} & -\Delta t \mathbf{H}^n \end{bmatrix} \begin{bmatrix} \mathbf{U} \\ \mathbf{P} \end{bmatrix}^n - \begin{bmatrix} \mathbf{F} \\ \Delta t \mathbf{S} \end{bmatrix}^n$$
(B5)

$$\mathbf{J}^n = \begin{bmatrix} \mathbf{K} & -\mathbf{Q} \\ -\mathbf{Q}^T & -\Delta t \mathbf{H}^n \end{bmatrix}$$
(B6)

Thus, the displacement \mathbf{U} and the fluid pressure \mathbf{P} can be updated by

$$\begin{bmatrix} \mathbf{U} \\ \mathbf{P} \end{bmatrix}^{n+1} = \begin{bmatrix} \mathbf{U} \\ \mathbf{P} \end{bmatrix}^n - \frac{\mathbf{R}^n}{\mathbf{J}^n}$$
(B7)

The convergence criterion for the fluid-solid coupling iteration can be written as

$$\begin{cases} \eta_p = \|\mathbf{P}^{n+1} - \mathbf{P}^n\| / \|\mathbf{P}^n\| \leq \varepsilon_{tol}^p \\ \eta_w = \|\mathbf{w}^{n+1} - \mathbf{w}^n\| / \|\mathbf{w}^n\| \leq \varepsilon_{tol}^w \end{cases}$$
(B8)

where \mathbf{w}^n is the fracture width at the n th iteration step. The tolerance ε_{tol}^p and ε_{tol}^w are taken as 0.05 and 0.01, respectively, in this paper.

References

Belytschko, T., Black, T., 1999. Elastic crack growth in finite elements with minimal remeshing. *Int. J. Numer. Meth. Eng.* 45 (5), 601–620.

Beugelsdijk, L.J.L., de Pater, C.J., Sato, K., 2000. Experimental hydraulic fracture propagation in a multi-fractured medium. In: *SPE Asia Pacific Conference on Integrated Modelling for Asset Management*, 25–26 April. Society of Petroleum Engineers, Yokohama, Japan.

Blanton, T.L., 1982. An experimental study of interaction between hydraulically induced and pre-existing fractures. In: *SPE Unconventional Gas Recovery Symposium*, 16–18 May. Society of Petroleum Engineers, Pittsburgh, Pennsylvania.

Blanton, T.L., 1986. Propagation of hydraulically and dynamically induced fractures in naturally fractured reservoirs. In: *SPE Unconventional Gas Technology Symposium*, 18–21 May. Society of Petroleum Engineers, Louisville, Kentucky.

Budyn, E., Zi, G., Moes, N., Belytschko, T., 2004. A method for multiple crack growth in brittle materials without remeshing. *Int. J. Numer. Meth. Eng.* 61 (10), 1741–1770.

Chen, Z., Jeffrey, R.G., Zhang, X., Kear, J., 2017. Finite-element simulation of a hydraulic fracture interacting with a natural fracture. *SPE J.* 22 (01), 219–234.

Chuprakov, D., Melchava, O., Prioul, R., 2013. Injection-sensitive mechanics of hydraulic fracture interaction with discontinuities. In: *47th U.S. Rock Mechanics/Geomechanics Symposium*, 23–26 June. American Rock Mechanics Association, San

- Francisco, California.
- Dahi-Taleghani, A., Olson, J.E., 2011. Numerical modeling of multistranded-hydraulic-fracture propagation: accounting for the interaction between induced and natural fractures. *SPE J.* 16 (3), 575–581.
- Dahi-Taleghani, A., Olson, J.E., 2014. How natural fractures could affect hydraulic-fracture geometry. *SPE J.* 19 (1), 161–171.
- Damjanac, B., et al., 2010. A new approach to hydraulic fracturing modeling in naturally fractured reservoirs. In: 44th U.S. Rock Mechanics Symposium and 5th U.S.-Canada Rock Mechanics Symposium, 27–30 June. American Rock Mechanics Association, Salt Lake City, Utah.
- Daneshy, A.A., 1974. Hydraulic fracture propagation in the presence of planes of weakness. In: SPE European Spring Meeting, 29–30 May. Society of Petroleum Engineers, Amsterdam, Netherlands.
- Daux, C., Moes, N., Dolbow, J., Sukumar, N., Belytschko, T., 2000. Arbitrary branched and intersecting cracks with the extended finite element method. *Int. J. Numer. Meth. Eng.* 48 (12), 1741–1760.
- De Pater, C.J., Beugelsdijk, L.J.L., 2005. Experiments and numerical simulation of hydraulic fracturing in naturally fractured rock, Alaska Rocks 2005. In: The 40th U.S. Symposium on Rock Mechanics (USRMS), 25–29 June. American Rock Mechanics Association, Anchorage, Alaska.
- Erdogan, F., Sih, G.C., 1963. On the crack extension in plates under plane loading and transverse shear. *J. Basic Eng.* 85 (4), 519–525.
- Gonzalez-Chavez, M., Dahi Taleghani, A., Olson, J.E., 2015. A cohesive model for modeling hydraulic fractures in naturally fractured formations. In: SPE Hydraulic Fracturing Technology Conference, 3–5 February. Society of Petroleum Engineers, The Woodlands, Texas, USA.
- Gu, H., Weng, X., 2010. Criterion for fractures crossing frictional interfaces at non-orthogonal angles. In: 44th U.S. Rock Mechanics Symposium and 5th U.S.-Canada Rock Mechanics Symposium, 27–30 June. American Rock Mechanics Association, Salt Lake City, Utah.
- Gu, H., et al., 2011. Hydraulic fracture crossing natural fracture at non-orthogonal angles, a criterion, its validation and applications. In: SPE Hydraulic Fracturing Technology Conference, 24–26 January. Society of Petroleum Engineers, The Woodlands, Texas, USA.
- Guo, J., Zhao, X., Zhu, H., Zhang, X., Pan, R., 2015. Numerical simulation of interaction of hydraulic fracture and natural fracture based on the cohesive zone finite element method. *J. Nat. Gas Sci. Eng.* 25, 180–188.
- He, M.-Y., Hutchinson, J.W., 1989. Crack deflection at an interface between dissimilar elastic materials. *Int. J. Solid Struct.* 25 (9), 1053–1067.
- Jang, Y., Kim, J., Ertekin, T., Sung, W., 2016. Fracture propagation model using multiple planar fracture with mixed mode in naturally fractured reservoir. *J. Petrol. Sci. Eng.* 144, 19–27.
- Jeffrey, R.G., et al., 2015. A 2D experimental method with results for hydraulic fractures crossing discontinuities. In: 49th U.S. Rock Mechanics/Geomechanics Symposium, 28 June–1 July. American Rock Mechanics Association, San Francisco, California.
- Khoei, A.R., Hirmant, M., Vahab, M., Bazargan, M., 2015. An enriched FEM technique for modeling hydraulically driven cohesive fracture propagation in impermeable media with frictional natural faults: numerical and experimental investigations. *Int. J. Numer. Meth. Eng.* 104 (6), 439–468.
- Kresse, O., Weng, X., Gu, H., Wu, R., 2013. Numerical modeling of hydraulic fractures interaction in complex naturally fractured formations. *Rock Mech. Rock Eng.* 46 (3), 555–568.
- Lamont, N., Jessen, F.W., 1963. The effects of existing fractures in rocks on the extension of hydraulic fractures. *J. Petrol. Technol.* 15 (2), 203–209.
- Liu, C., Liu, H., Zhang, Y., Deng, D., Wu, H., 2015. Optimal spacing of staged fracturing in horizontal shale-gas well. *J. Petrol. Sci. Eng.* 132, 86–93.
- Liu, C., et al., 2016. Optimal spacing of sequential and simultaneous fracturing in horizontal well. *J. Nat. Gas Sci. Eng.* 29, 329–336.
- Moes, N., Dolbow, J., Belytschko, T., 1999. A finite element method for crack growth without remeshing. *Int. J. Numer. Meth. Eng.* 46 (1), 131–150.
- Nagel, N.B., Gil, I., Sanchez-Nagel, M., Damjanac, B., 2011. Simulating hydraulic fracturing in real fractured rock-overcoming the limits of pseudo-3D models. In: SPE Hydraulic Fracturing Technology Conference, 24–26 January. Society of Petroleum Engineers, The Woodlands, Texas, USA.
- Nuismer, R., 1975. An energy release rate criterion for mixed mode fracture. *Int. J. Fract.* 11 (2), 245–250.
- Olson, J.E., Bahorich, B., Holder, J., 2012. Examining hydraulic fracture-natural fracture interaction in hydrostone block experiments. In: SPE Hydraulic Fracturing Technology Conference, 6–8 February. Society of Petroleum Engineers, The Woodlands, Texas, USA.
- Olson, J.E., Taleghani, A.D., 2009. Modeling simultaneous growth of multiple hydraulic fractures and their interaction with natural fractures. In: SPE Hydraulic Fracturing Technology Conference, 19–21 January. Society of Petroleum Engineers, The Woodlands, Texas.
- Omid, O., Abedi, R., Enayatpour, S., 2015. An adaptive meshing approach to capture hydraulic fracturing. In: 49th U.S. Rock Mechanics/Geomechanics Symposium, 28 June–1 July. American Rock Mechanics Association, San Francisco, California.
- Potluri, N.K., Zhu, D., Hill, A.D., 2005. The effect of natural fractures on hydraulic fracture propagation. In: SPE European Formation Damage Conference, 25–27 May. Society of Petroleum Engineers, Sheveningen, The Netherlands.
- Ren, L., et al., 2016. Modeling and simulation of complex fracture network propagation with SRV fracturing in unconventional shale reservoirs. *J. Nat. Gas Sci. Eng.* 28, 132–141.
- Renshaw, C.E., Pollard, D.D., 1995. An experimentally verified criterion for propagation across unbounded frictional interfaces in brittle, linear elastic-materials. *Int. J. Rock Mech. Min. Sci. Geomech. Abstr.* 32 (3), 237–249.
- Shi, F., Wang, X., Liu, C., Liu, H., Wu, H., 2016. A coupled extended finite element approach for modeling hydraulic fracturing in consideration of proppant. *J. Nat. Gas Sci. Eng.* 33, 885–897.
- Shi, F., Wang, X., Liu, C., Liu, H., Wu, H., 2017. An XFEM-based method with reduction technique for modeling hydraulic fracture propagation in formations containing frictional natural fractures. *Eng. Fract. Mech.* 173, 64–90.
- Stolarska, M., Chopp, D.L., Moes, N., Belytschko, T., 2001. Modelling crack growth by level sets in the extended finite element method. *Int. J. Numer. Meth. Eng.* 51 (8), 943–960.
- Wang, X., Liu, C., Wang, H., Liu, H., Wu, H., 2016a. Comparison of consecutive and alternate hydraulic fracturing in horizontal wells using XFEM-based cohesive zone method. *J. Petrol. Sci. Eng.* 143, 14–25.
- Wang, X., Shi, F., Liu, H., Wu, H., 2016b. Numerical simulation of hydraulic fracturing in orthotropic formation based on the extended finite element method. *J. Nat. Gas Sci. Eng.* 33, 56–69.
- Warpinski, N.R., Teufel, L.W., 1987. Influence of geologic discontinuities on hydraulic fracture propagation. *J. Petrol. Technol.* 39 (2), 209–220.
- Wasantha, P.L.P., Konietzky, H., 2016. Fault reactivation and reservoir modification during hydraulic stimulation of naturally-fractured reservoirs. *J. Nat. Gas Sci. Eng.* 34, 908–916.
- Weng, X., et al., 2014. Applying complex fracture model and integrated workflow in unconventional reservoirs. *J. Petrol. Sci. Eng.* 124, 468–483.
- Weng, X., Kresse, O., Cohen, C.E., Wu, R., Gu, H., 2011. Modeling of hydraulic fracture network propagation in a naturally fractured formation. In: SPE Hydraulic Fracturing Technology Conference, 24–26 January. Society of Petroleum Engineers, The Woodlands, Texas, USA.
- Wu, K., Olson, J.E., 2015. Mechanics analysis of interaction between hydraulic and natural fractures in shale reservoirs. In: Unconventional Resources Technology Conference, 25–27 August. Unconventional Resources Technology Conference, Denver, Colorado, USA.
- Xie, L., Min, K.-B., Shen, B., 2016. Simulation of hydraulic fracturing and its interactions with a pre-existing fracture using displacement discontinuity method. *J. Nat. Gas Sci. Eng.* 36 (B), 1284–1294.
- Zeng, Q., Yao, J., 2016. Numerical simulation of fracture network generation in naturally fractured reservoirs. *J. Nat. Gas Sci. Eng.* 30, 430–443.
- Zhang, X., Jeffrey, R.G., 2006. The role of friction and secondary flaws on deflection and re-initiation of hydraulic fractures at orthogonal pre-existing fractures. *Geophys. J. Int.* 166 (3), 1454–1465.
- Zhang, X., Jeffrey, R.G., 2012. Fluid-driven multiple fracture growth from a permeable bedding plane intersected by an ascending hydraulic fracture. *J. Geophys. Res.-Solid Earth* 117, B12402.
- Zhang, X., Jeffrey, R.G., 2014. Role of overpressurized fluid and fluid-driven fractures in forming fracture networks. *J. Geochem. Explor.* 144, 194–207.
- Zhang, X., Jeffrey, R.G., Thiercelin, M., 2009. Mechanics of fluid-driven fracture growth in naturally fractured reservoirs with simple network geometries. *J. Geophys. Res.-Solid Earth* 114, B12406.
- Zhou, J., Chen, M., Jin, Y., Zhang, G.-q., 2008. Analysis of fracture propagation behavior and fracture geometry using a tri-axial fracturing system in naturally fractured reservoirs. *Int. J. Rock Mech. Min. Sci.* 45 (7), 1143–1152.
- Zou, Y., Zhang, S., Ma, X., Zhou, T., Zeng, B., 2016. Numerical investigation of hydraulic fracture network propagation in naturally fractured shale formations. *J. Struct. Geol.* 84, 1–13.